Fabric, texture, and bubble characteristics of the million-year old Allan Hills blue ice core ALHIC1901

Nicolas Stoll[1,2,3], Marguerite Shaya[1], Liam Kirkpatrick[1], Johannes Freitag[3], Valens Hishamunda[4], John-Morgan Manos[1], Daniela Jansen[3], Ilka Weikusat[3,5], John Fegyveresi[6], Bradley Paul Lipovsky[1], Ed Brook[7], Sarah Shackleton[4,8], John Higgins[4], and T. J. Fudge[1]

[1]Department of Earth and Space Sciences, University of Washington, Seattle, WA, USA
[2]Department of Environmental Sciences, Informatics and Statistics, Ca'Foscari University of Venice, Venice, Italy
[3]Department of Geosciences, Alfred Wegener Institute Helmholtz Centre for Polar and Marine Research, Bremerhaven, Germany
[4]Department of Geosciences, Princeton University, Princeton, NJ, USA
[5]Geoscience Department, Eberhard Karls University, T¨ubingen, Germany
[6]School of Earth and Sustainability, Northern Arizona University, AZ, USA
[7]College of Earth, Ocean, and Atmospheric Sciences, Oregon State University, Corvallis, OR, USA
[8]Department of Geology & Geophysics, Woods Hole Oceanographic Institution, Woods Hole, MA, USA

Contact: Nicolas Stoll (nicolas.stoll@awi.de)

This is a non-peer reviewed preprint submitted to EarthArXiv. The manuscript has been submitted for peer review to *JGR: Solid Earth*.

Fabric, texture, and bubble characteristics of the million-year old Allan Hills blue ice core ALHIC1901

Nicolas Stoll[1,2,3], Marguerite Shaya[1], Liam Kirkpatrick[1], Johannes Freitag[3], Valens Hishamunda[4], John-Morgan Manos[1], Daniela Jansen[3], Ilka Weikusat[3,5], John Fegyveresi[6], Bradley Paul Lipovsky[1], Ed Brook[7], Sarah Shackleton[4,8], John Higgins[4], and T. J. Fudge[1]

[1]Department of Earth and Space Sciences, University of Washington, Seattle, WA, USA
[2]Department of Environmental Sciences, Informatics and Statistics, Ca'Foscari University of Venice, Venice, Italy
[3]Department of Geosciences, Alfred Wegener Institute Helmholtz Centre for Polar and Marine Research, Bremerhaven, Germany
[4]Department of Geosciences, Princeton University, Princeton, NJ, USA
[5]Geoscience Department, Eberhard Karls University, Tübingen, Germany
[6]School of Earth and Sustainability, Northern Arizona University, AZ, USA
[7]College of Earth, Ocean, and Atmospheric Sciences, Oregon State University, Corvallis, OR, USA
[8]Department of Geology & Geophysics, Woods Hole Oceanographic Institution, Woods Hole, MA, USA

Key Points:

- First characterization of fabric, texture, and 2D and 3D bubble characteristics in four depth regimes around identified age reversals from the ALHIC1901 blue ice core from Allan Hills, Antarctica
- Multi-method approach shows strongly elongated air bubbles, indications of dynamic recrystallization, simple shear as the main deformation type and the common occurrence of "stripes", i.e., differently oriented crystals
- Kink bands and z-folds identified as potential reasons for a disturbed stratigraphy and distinct bubble characteristics indicating the alteration of the original bubbles and their gas content

Corresponding author: Nicolas Stoll, nicolas.stoll@awi.de

Abstract

Ice cores from the Allan Hills blue ice area in Antarctica have been dated to several million years of age. However, the stratigraphy of these cores is often disturbed, and age reversals are common, hampering the interpretation of the derived climate records. To better understand the physical processes affecting the ice, we here use a variety of microstructural methods to investigate the fabric, texture and bubble characteristics of four depth regimes in the ALHIC1901 core. We find single maximum CPOs with an occasional second maximum; stripes of differently orientated crystals are common. We further observe small, potentially elongated, grains containing indications of dynamic recrystallisation. 2D and 3D bubble data show strongly elongated bubbles and very low bubble number densities compared to similar depths of deep ice cores. We interpret these findings as indications of simple shear, including kink and z-folds at the centimeter scale and potential alterations to the original air bubbles and, thus, their gas content. Extended studies of Allan Hills ice cores using continuous sections are needed to evaluate the spatial scale of the folding and its impact on the climate record.

1 Introduction

Reconstructing the palaeoclimate from air bubbles and chemical impurities preserved in ice cores relies heavily on continuous records and thus an undisturbed stratigraphy (e.g., EPICA Community Members, 2004; Lüthi et al., 2008). Undisturbed records are vital for the small number of deep ice cores going back several hundred thousand years, such as Dome Fuji (Dome Fuji Ice Core Project Members: et al., 2017), Vostok (Petit et al., 1999), and EPICA Dome C (EPICA Community Members, 2004). However, disturbed records can be identified and reconstructed to a certain extent by, among others, identifying folding and the main deformation type (NEEM community members, 2013). The International Partnership in Ice Core Sciences (IPICS) has formulated the quest to investigate the Mid-Pleistocene Transition (MPT) by retrieving continuous ice core records spanning the last 1.5 Myr (Fischer et al., 2013; Wolff et al., 2022). Worldwide, several projects have commenced on this journey, focusing on different Antarctic locations and approaches united by the goal to find million-year-old ice. Rather than pursing ice-core projects that necessitate multi-year drilling campaigns, Higgins et al. (2015) and Yan et al. (2019) carried out a different strategy. They explored Antarctic ice of up to 2 Myrs of age originating from the Allan Hills (AH) Blue Ice Area (BIA) on the western flanks of the Transantarctic Mountains in Victoria Land.

BIAs are specific features of the polar regions characterized by particular glaciological and meteorological conditions, such as net ablation through sublimation and strong winds. In some parts of BIAs, very old ice is available at shallow depths (Bintanja, 1999; Sinisalo & Moore, 2010). In Antarctica, BIAs cover roughly one per cent of the total area (Bintanja, 1999) and have been mainly of interest for finding meteorites (Yoshida et al., 1971). The AH BIA is characterized by unusual glaciological conditions, i.e., an ascending movement of ice, which is assumed to be caused by upward flow over the submerged nunatak, resulting in ice layers dipping with up to 69° (Kirkpatrick et al., 2025). On the surface, strong sublimation reveals layer by layer, making it possible to find old ice at shallow depths (∼200 m). The AH BIA provides snapshots into the distant past spanning the Miocene and Pliocene (Shackleton, Hishamunda, Davidge, et al., 2025) and offering novel insights into past conditions, such as global ocean heat content (Shackleton, Hishamunda, Yan, et al., 2025), CO_2 and CH_4 levels (Peterson et al., 2025), and the extent of the Antarctic ice sheet (Shackleton, Hishamunda, Davidge, et al., 2025).

Some AH cores, such as ALHIC1901, exhibit distinct age reversals with depth (Shackleton, Hishamunda, Davidge, et al., 2025) rather than the continuous depth-age relationship aimed for in most deep ice cores (e.g. North Greenland Ice Core Project members, 2004; EPICA Community Members, 2004; Dome Fuji Ice Core Project Members: et al., 2017). These age reversals, and the strong layer dipping (Kirkpatrick et al., 2025), suggest a disturbed stratigraphy, which hampers the interpretation of the data and warrants further investigation. The discontinuous records underscore the need to develop a deeper understanding of the ice dynamics and deformation in the AH BIA needed to exploit the full potential of the preserved ice. Analyzing the physical properties, such as grain size and shape and crystal-preferred-orientation (CPO), has become standard procedure for major ice core projects (e.g., R. B. Alley et al., 1995; Thorsteinsson et al., 1997; Montagnat et al., 2014; Fitzpatrick et al., 2014; Weikusat et al., 2017; Stoll et al., 2025).

Here, we conduct the first microstructural characterization of AH ice by analyzing four depth regimes from the ALHIC1901 core using various methods on the same samples. We investigate solid ice samples in terms of their 1) texture, including bubble properties and the size and shape of ice crystals, and 2) CPO, also called crystal fabric, which provides insights into their deformational behavior. These insights into the ice dynamics at the ALHIC1901 site are crucial for a comprehensive understanding of the AH climate records. Insights from ALHIC1901 will also be important for interpreting the deepest layers of other million-year ice core records, which are likely to be disturbed close to bedrock.

2 Materials and Methods

2.1 Working area and the ALHIC1901 ice core

The ALHIC1901 core, dry-drilled in the Allan Hills of Antarctica during the 2019-2020 season, is located at 76.73° S, 159.356° E, at an elevation of 1992 m (Fig. 1a). The modern horizontal surface velocity in the area is a few centimeters per year (Spaulding et al., 2012) with ∼8 cm/year close to ALHIC1901 derived by GPS stake measurements. Upstream velocities are slightly faster (Fig. 1a). The core has a diameter of 24 cm and a length of 159.84 m, almost reaching bedrock. Core quality upon recovery varied greatly, and was often noted as "poor," indicating multiple fractures, spalls and internal cracks or breaks within the core. True azimuthal core orientations were not documented during the drilling, and for some samples, the relative orientations to the core axis are also not available. Temperature with depth was recorded via Distributed Temperature Sensing (DTS) in 2022, 2023 and 2024 and is displayed in Fig. 1b.

$^{40}Ar_{atm}$ dating using established protocols (Bender et al., 2008; Yan et al., 2019) of ALHIC1901 shows a maximum age of 4.0 ±0.4 Ma close to bedrock (159 m) with a complex age-depth relationship, several instances of inverted stratigraphy, and discontinuities in the record (see Shackleton, Hishamunda, Davidge, et al. (2025) for details). Argon dates are averages from discrete measurements of large samples (500-600 g). Thus, derived ages potentially do not represent small-scale details of the depth-age relationship.

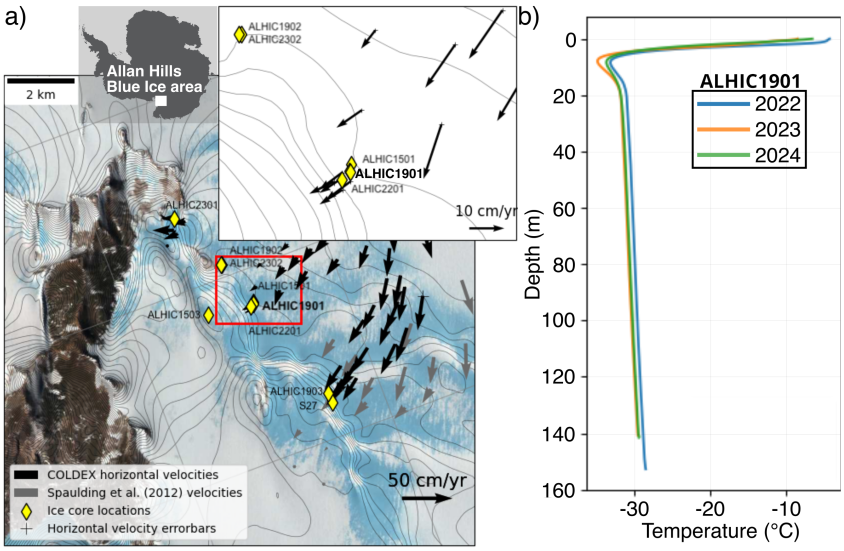

Figure 1. a) Map of the Allan Hills Blue Ice area, Antarctica (indication not to scale) and horizontal surface flow velocities. Ice core locations are indicated with markers; the analyzed ALHIC1901 core is emphasized in bold. b) Distributed Temperature Sensing (DTS) measurements with depth of the ALHIC1901 site (one measurement per year).

2.2 Samples

At the NSF Ice Core Facility (NSF-ICF, -26°C) in Denver, Colorado, we cut samples from the main core within the limitations of ice core availability and quality. Sample availability and shape are constrained and many samples are streaked by internal cracks, limiting the microstructural analysis possibilities. Previously argon-dated samples were often expended for dating and other analyses. Thus, some of our indicated ages are estimates based on adjacent, dated samples (Table 1). Due to potential steep layering in the ice Kirkpatrick et al. (2025), these age estimates have to be treated with caution. We selected four depth regimes (∼141 m, ∼144 m, ∼151 m, ∼155 m) close to known age reversals (Table 1 and Shackleton, Hishamunda, Davidge, et al. (2025)) for this study. We targeted horizontally oriented samples, as far as possible, from any visually undisturbed sections of the core to ensure reliable data. We attempted to prepare ideal section cut dimensions of 6 x 10 cm for our targeted samples, but sample shape and size vary slightly. We cut four adjacent vertical sections from the deepest sample, 228_4, in a 2 x 2 pattern covering an area of ∼0.04 m^2. Additional adjacent samples were cut for complementary 3D analyses at the Alfred Wegener Institute Helmholtz Centre for Polar and Marine Research, Bremerhaven, Germany (AWI) (see below).

Table 1. Overview of ALHIC1901 samples and 2D bubble data. Samples analyzed in 3D are indicated in bold, details are displayed in Table C1. The depth refers to the sample's vertical midpoint. Ages are derived from $^{40}Ar_{atm}$ dating and have an uncertainty of ±11%.

Sample	Depth	Age (myr)*	Orientation	Bubbles (n)	Bubbles ≥0.5 mm^2 (n)
210_2	141.48	∼0.66	horizontal	1241	337
210_4	141.68	0.88	horizontal	605	261
210_6	141.90	1.14	horizontal	1195	358
210_7	142.19	∼1.4	horizontal	986	396
211_2	142.35	∼0.82	horizontal	1271	359
214_3	144.84	∼2.3	horizontal	408	158
214_4	144.88	1.6	horizontal	621	274
214_5	145.00	2	horizontal	843	318
214_6	145.21	1.6	horizontal	1130	430
214_7	145.32	1.2	horizontal	1053	490
222_1	151.00	∼0.7	horizontal	1379	455
222_2	151.14	∼0.7	horizontal	866	211
223_1	151.89	∼2	horizontal	1152	291
223_3	152.11	∼2	horizontal	1605	324
228_4	155.09	∼1.3	horizontal	1768	305
228_4_1a	155.16	∼1.6	vertical	1706	89
228_4_1b	155.16	∼1.6	vertical	-	-
228_4_2a	155.26	∼1.6	vertical	1824	100
228_4_2a	155.26	∼1.6	vertical	-	-
Total	-	-	-	19,653	5,156

* ∼ marks best age estimate from $^{40}Ar_{atm}$ dating at respective depth regime.

2.3 2D Bubble Analysis at NSF-ICF

Eighteen samples were polished from both sides with a Leica microtome until the samples were 0.5 cm thick (-26°C). From here on, we refer to these samples as *bubble sections*. Following the method described in J. M. Fegyveresi et al. (2019), bubble sections were placed on an illuminated movable high-precision table and photographed with a stationary Nikon D80 single reflex camera and Nikon 105 mm f/2.8D lens using a focal length of 105 mm and an aperture of 13. Depending on sample size and geometry, between 21 and 44 single images were taken per sample.

Single images were stitched together into a high-resolution image using *Adobe Lightroom Classic*; we refer to the resulting images as *bubble images* (2). Bubble images were semi-automatically edited within *Adobe Photoshop 2024* using the Magic Wand tool and

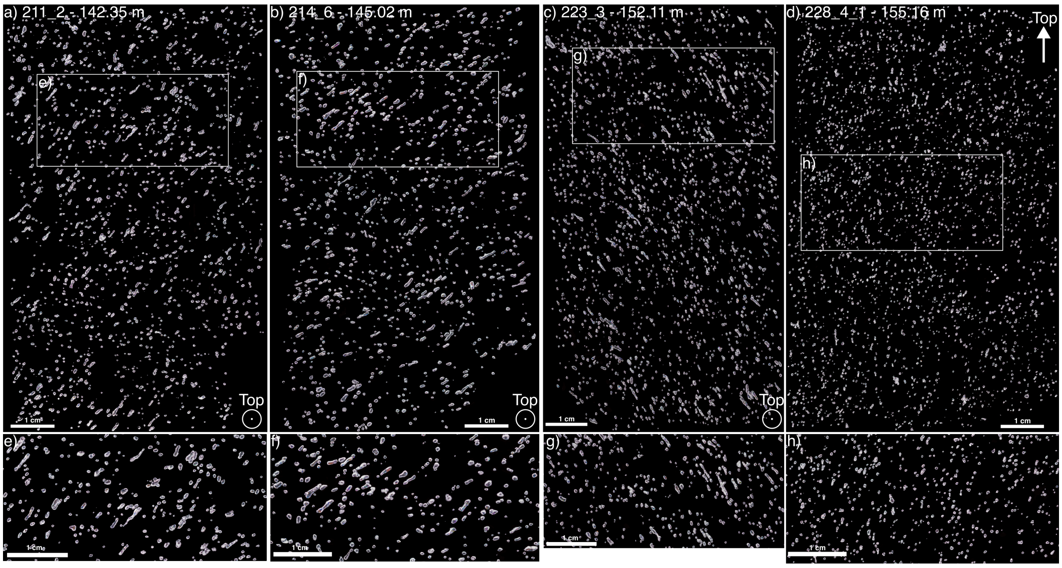

Figure 2. Bubble images for horizontal samples a) 211_2, b) 214_6, c) 223_3 and vertical sample d) 228_4_1. Detailed views are indicated and displayed in e)-h) showing highly elongated bubbles. Top indicates the ice sheet surface.

manual selections to remove optical artifacts, including reflections, scratches from microtoming, internal ice cracks, and out-of-focus bubbles. Bubbles were then digitally separated from the background. Bubbles at the sample edges were also excluded from the analysis. We used the open-source software *FIJI ImageJ* for bubble identification via thresholding and the bubble properties analysis. To eliminate tiny artifacts potentially missed during data processing, only objects interpreted as bubbles with a minimum area of 0.1 mm^2 were analyzed regarding area and aspect ratio. Aspect ratio is the ratio of the longest to the shortest axis of an ellipsoid, i.e., a measure for the elongation of a bubble (1=perfectly round, $\geq$1=elongated). However, depending on the bubble elongation and sample cutting plane, 2D measurements might underrepresent aspect ratios. We thus validate 2D measurements with additional 3D measurements (see section 2.4.3). A common parameter to measure is bubble number density. However, for the 2D measurements, this is not feasible due to the often poor ice quality. We only analyzed the plane in focus and often had to digitally remove certain areas containing microcracks within the samples, which limits and biases the analyzable area. Bubble number density is thus only investigated for samples analyzed in 3D 2.4.3).

2.4 Texture, CPO and 3D Bubble Analysis at AWI

We transported the bubble sections and adjacent samples in a commercially available insulated shipping box (Credo Cube Series 20M 56L) at below -20°C to AWI, Bremerhaven, Germany. The samples were stored at -30°C until further analysis shortly after shipping. No sample showed indications of melting after the transport.

2.4.1 Texture Measurements

In the AWI cold laboratory (-20°C), previously analyzed bubble sections were re-polished with a Leica microtome, taking off as little ice as possible (between 50 and 100 µm). We refer to these samples as *thick sections*. Thick sections underwent a controlled sublimation of 1.5-2 hours, depending on the sample, to enhance the visibility of microstructural features, such as (sub–) grain boundaries.

Thick sections were analyzed with the Schäfter+Kirchhoff GmbH Large Area Scanning Macroscope (LASM) utilizing a line scan camera and direct bright-field illumination (Binder et al., 2013; Krischke et al., 2015). The sample moves at a constant velocity relative to the sensor, while individual line signals are recorded with a resolution of 8192 pixels. Light is reflected differently back to the sensor from parallel areas and tilted features. Thus, features such as grain boundaries appear dark. Due to the previous bubble analysis, samples were relatively thin (∼0.5 cm), and the grain boundary network on the backside of the samples appeared as blurry black lines in the image. This overprint and internal microcracks prohibit a quantitative analysis of these thick sections.

2.4.2 CPO Measurements and Data Processing

After LASM measurements, samples were polished to a thickness of 0.3 mm, resulting in *thin sections* for CPO analysis. We utilized the Russel-Head Instruments G50 Fabric Analyzer (C. J. Wilson et al., 2003). The setup automatically measures the orientation of the main crystallographic axis, the c-axis. We applied a 20 µm spot size and measurements took between 30 and 60 min, depending on the sample dimensions. We refer to Stoll et al. (2025) for a more detailed description.

We manually corrected the raw image data to exclude artifacts, such as cracks and artificial ice crystals from water-gluing the sample onto the plate. We applied the software *cAxes* (Eichler, 2013) to analyze all grains above 500 pixels or 0.2 mm^2 in size with the same threshold criteria as Stoll et al. (2025), deriving information on grain size and CPO. We calculate the eigenvalues of the second-order orientation tensor and Woodcock parameter, a measure to differentiate between girdle and single maximum CPOs, following standard structural geology methods (Wallbrecher, 1986). The c-axes distribution can be displayed as an ellipsoid whose axes are represented by the invariant eigenvalues (e_1, e_2, e_3), which are usually normalized (λ_1, λ_2, and λ_3) obeying $\lambda_1+\lambda_2+\lambda_3=1$ and $\lambda_1 \leq \lambda_2 \leq \lambda_3$ (Woodcock, 1977). We furthermore display the Woodcock parameter, which quantifies the shape of a c-axis orientation distribution enabling to distinguish between girdle (> 1) and single-maximum (< 1) CPOs (Woodcock, 1977).

2.4.3 3D Bubble Analysis via 3D X-ray-microfocus Computer Tomography

To investigate bubble properties in 3D and evaluate our 2D bubble data, we selected 10 additional ALHIC1901 samples (210_4, 214_3, 214_4, two different sections of 214_5, 222_1 and 228_4; details in Table C1) adjacent to previously characterized bubble sections. These samples had larger volumes than the already measured sections and were thus suitable for the analysis with the AWI ice computer tomograph (CT, see Freitag et al. (2013) for details). The unique AWI X-ray microfocus CT is housed in a dedicated cold laboratory (-15°C) and produces high-resolution cross-section grayscale-coded intensity images ("radioscopic images") of snow, firn, or bubbly ice cores of up to 100 cm length. The CT is non-destructive, operates an X-ray source at 140 kV and 200 µA, and uses a 2000x4000-pix detector. The field of view is 12 cm, enabling the combined measurement of up to 5 ice samples per run. Resolutions of up to 2 µm are possible; however, due to the increasing measurement time, we chose a spatial resolution of 30 µm to reconstruct the sample's 3D structure.

We applied a beam hardening correction, denoising by median filtering (3x3x3), segmentation by global thresholding and 3D-object labeling (26-neighbor definition). The data set was cleaned by rejecting all identified pore objects smaller than 20 voxels. We here focus on bubble number density, bubble size and aspect ratio.

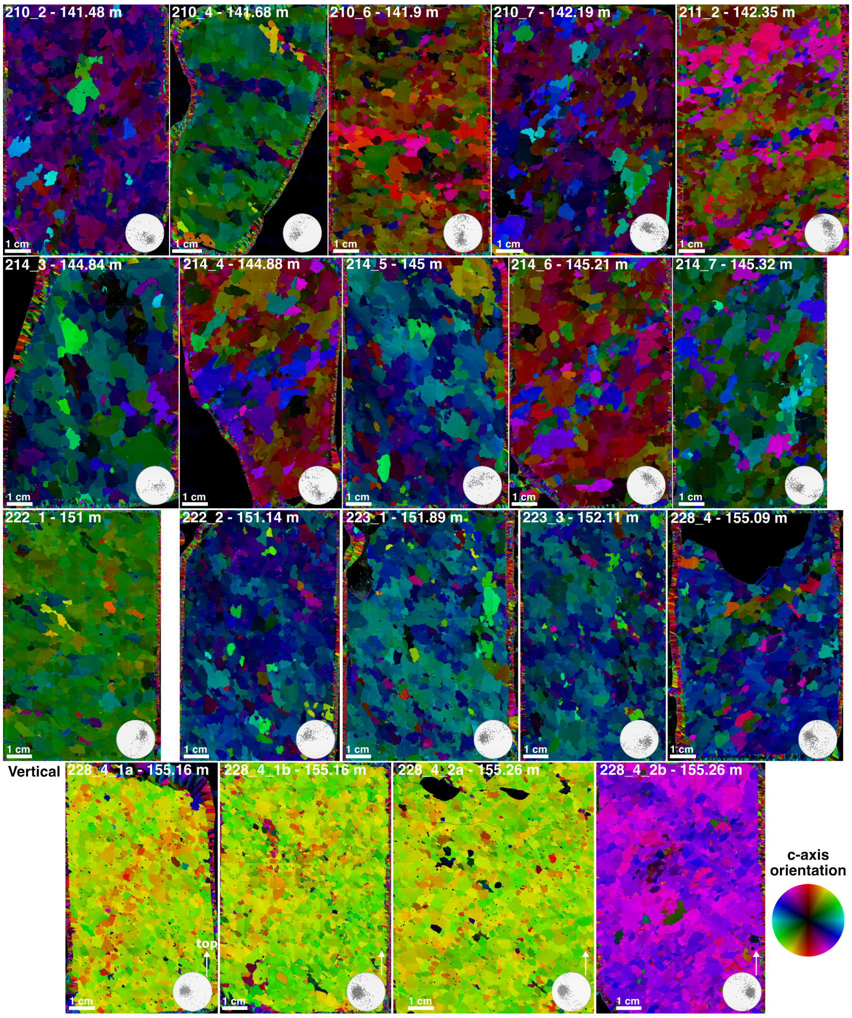

Figure 3. Microstructure with color-coded c-axis orientations and stereo-plots (lower-hemisphere Schmidt equal-area projection) for all samples. The last four samples are vertical sections and horizontally adjacent to each other. Sample 1a and 1b are above 2a and 2b. 228_4_2b is mirrored along the vertical axis, thus the difference in the color scale. C-axis orientation is relative to the sample plane. Top indicates the ice sheet surface.

3 Results

3.1 Fabric - CPO Patterns and Statistical Parameters

We display microstructure images of all samples with the corresponding CPOs in Fig. 3. A larger overview of CPOs is displayed in Fig. A1. All stereoplots show single maximum CPOs with a varying number of differently oriented crystals. The single maximum strength varies from fairly strong, i.e., most c-axes are oriented similar (e.g., 210_2, 221_1 and 228_4_2) to weak, i.e., c-axes are further spread out (e.g., 210_4, 210_6 and 228_4). Typically, the centers of symmetry of the c-axes maxima are displaced from the vertical core axis, i.e., the center of the fabric projection, by 13 to 38°. This dip from the vertical is between 13 and 29° and between 30 and 38° in the two shallower (141-145 m) and two deeper (151-156 m) depth regimes, respectively. Occasionally, a second maximum occurs (e.g.,210_7, 211_2 and 214_6). These double maxima CPOs can resemble a weak, partial tilted girdle CPO.

Most samples are characterized by crystals of similar orientation complemented by several individual crystals (called "wild" grains by R. B. Alley et al. (1997)) and bands of crystals of different orientation (Fig. 3) (called "stripes" by R. B. Alley et al. (1997)). These differently oriented bands can be of cm-thickness and are especially prominent in samples 210_4, 211_2, 214_6, 222_1 and 228_4. C-axes from crystals within these stripes produce the second maximum visible in some CPO patterns (Fig. 3 and A1).

The eigenvalues with depth are shown in Fig. 4a. λ_1 stays close to 0 for the entire probed depth regime. In the shallowest five samples λ_2 increases from 0.13 to 0.36 and fluctuates around 0.25 in the second depth regime (145 m). Between 151 and 152 m, λ_2 decreases to around 0.12 and remains there at the deepest sample at 155 m while λ_3 displays mirrored behavior with minimum and maximum values of 0.63 and 0.8, respectively. The four vertical sections (black squares in Fig. 4a) display the largest λ_3 values.

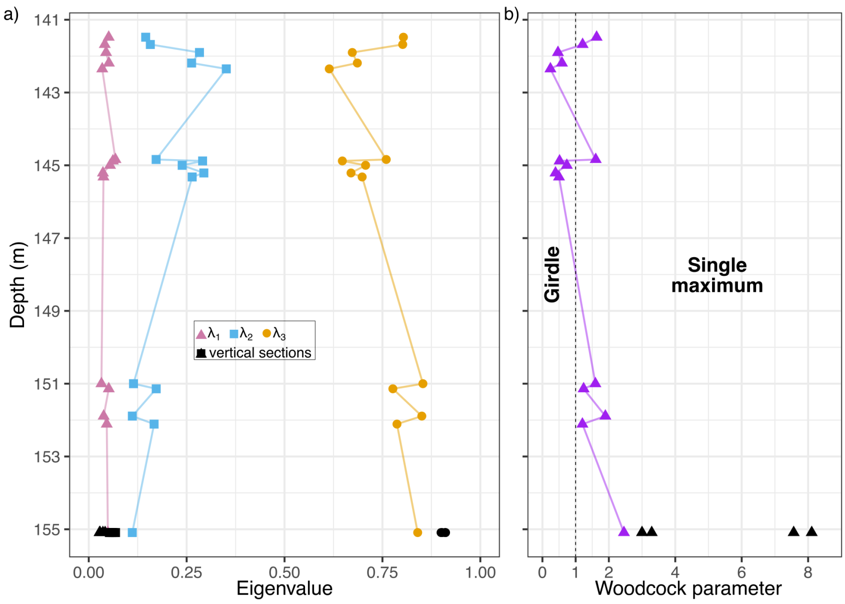

Figure 4. a) Eigenvalues with depth. Horizontal sections are displayed in color while vertical sections are black. b) Woodcock parameter with depth. Values above 1 represent single maximum CPOs, values below 1 indicate girdle CPOs.

The Woodcock parameter with depth is displayed in Fig. 4b). Values below and above 1 indicate girdle and single maximum CPOs, respectively. Around 142 and 145 m of depth, values fluctuate between 0 and 2 with distinct changes over centimeters. Below 151 m, the Woodcock parameter is always greater than 1 and increases with depth to above 8 (for two vertical sections). The Woodcock parameter in the deepest sample 228_4, consisting of one horizontal and four vertical sub-samples, displays strong differences depending on the sample location ("left" or "right" in vertical sections). Values for the "left samples" (228_4_1a and 228_4_2a) are between 7.5 and 8.1, while "right samples" (228_4_1b and 228_4_2b) are around 3.

3.2 Texture - Grain Size and Shape

The mean grain size (grain area derived from Fabric Analyzer data) per sample ranges from 6.9 to 23.3 mm^2 and 3.0 to 4.7 mm^2 for horizontal and vertical sections, respectively (Fig. 5a). The first five samples (around 142 m) show a continuous decrease in mean grain size with depth while the following five samples (around 145 m) alternate between 7 mm^2 and 23 mm^2. Grains around 151 m are slightly above 15 mm^2 and decrease slightly with depth to 8-13 mm^2 (152 m). The deepest samples, close to bedrock, display small overall grain sizes (below 8 mm^2). Grains in vertical sections (mean grain size between 3 and 4.8 mm^2) are significantly smaller than grains in horizontal section (mean grain size of 8.2 mm^2).

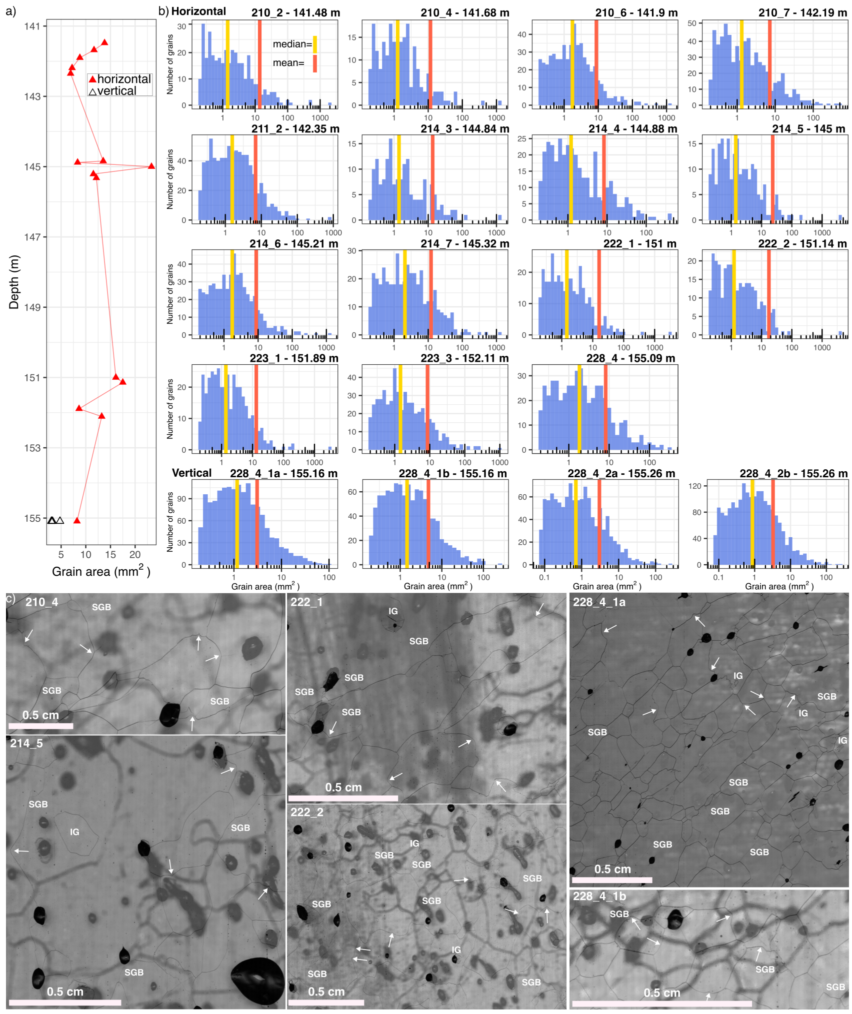

Figure 5. a) Grain size with depth; horizontal and vertical sections are indicated. b) Grain size distributions for every analyzed sample. Note the varying axes. c) Representative examples of microstructural features within six ALHIC1901 samples derived via LASM. Indicated are representative subgrain boundaries (SGB), island grains (IG) and grain boundaries protruding into neighboring grains (arrows). Blurry black lines are grain boundaries on the samples' backside. Different gray values are due to different capturing settings and changing light conditions. The dark area in 222_1 is caused by internal cracks below the focus plane.

The grain size distribution (Fig. 5b) displays skewed distributions with a tail towards larger grain sizes (minimum grain size: 0.2 mm^2). Mean values are always greater than the medians. The four vertical sections show the highest counts of small crystals and hardly contain large crystals, i.e., above 100 mm^2, which are present in all horizontal sections. We did not observe distinct grain-size contrasts, such as layers of fine-grained crystals.

Representative images of the texture, including subgrain boundaries, island grains (new grains formed inside distorted parent grains) and bulging grain boundaries, are displayed in Fig. 5c. Large grains in horizontal sections are often of amoeboid shape with bulging and intertwining grain boundaries (Fig. 3). Straight boundaries are rare while island grains and subgrain boundaries, arrays of dislocations (Weertman & Weertman, 1992), are common. Often, bubbles are surrounded by several small grains. Grain shapes in the four vertical sections (228_4) differ from horizontal sections. Here, grain boundaries tend to be more straight and grains sometimes show elongation and arrangement in preferred directions (228_4_1a and 228_4_1b in Fig. 5c).

LASM data show subgrain boundary types (normal, parallel and zig-zag after Weikusat et al. (2009)) of different intensities in all samples. Some subgrain boundaries cross entire grains. Examples of subgrain boundaries, bulging grain boundaries and other features, such as island grains, from various samples are displayed in Fig. 5c. As explained in Sect. 2.4.1, grain boundaries from the polished backside of the sample are visible in the images (e.g.,214_5, 222_2 and 228_4_1b in Fig. 5c).

3.3 2D Bubble Characteristics

We analyzed a total of 19,653 bubbles from 2D bubble images. Table 1 contains information about the samples and the number of analyzed bubbles. Four examples of bubble sections and respective close-ups are displayed in Fig. 2. To explore the impact of 2D bubble size (derived from pixel area), we set a threshold of 0.5 mm^2, which roughly equals the mean 2D area of all bubbles, for further analysis. About one quarter (5,156) of all bubbles are equal to or larger than 0.5 mm^2.

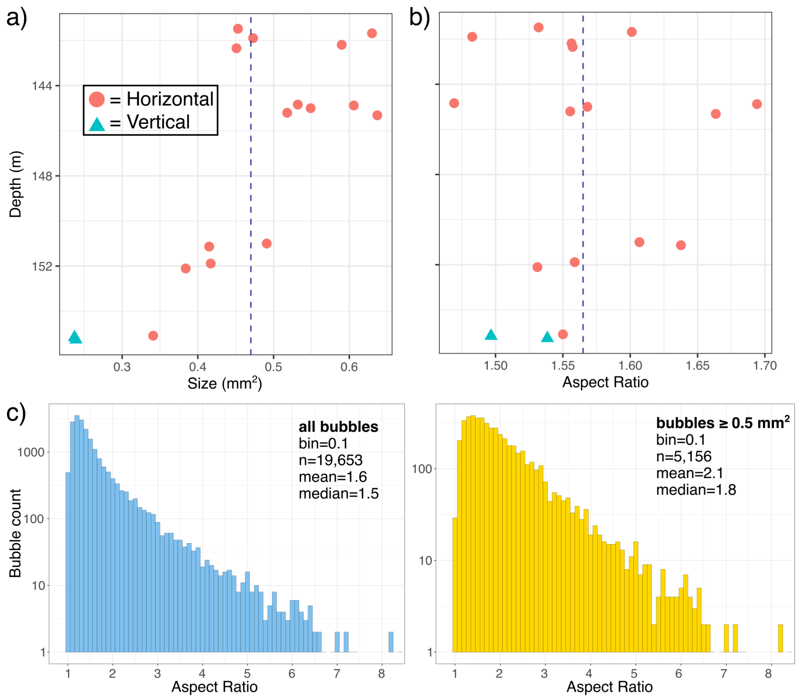

Figure 6. Mean values for 2D bubble a) size and b) aspect ratio with depth. The sample orientation is indicated as well as the overall mean (vertical dashed line). c) Histogram of aspect ratios for all analyzed 2D bubbles and bubbles of at least 0.5 mm^2.

The minimum bubble area is the applied threshold of 0.1 mm^2. The largest bubble has an area of 6.36 mm^2 (210_4). The mean bubble area per sample ranges from 0.24 mm^2 (228_4_1) to 0.64 (214_7), and the overall mean is 0.47 mm^2 (Fig. 6a). The mean bubble sizes in horizontal sections are 1.5 to 4 times larger than in vertical sections. Below 144 m, mean bubble size decreases with depth.

The mean aspect ratio per sample ranges from 1.47 (214_3) to 1.7 (214_4) (Fig. 6b). For all 19,653 bubbles, the median aspect ratio is 1.5 and the mean is 1.6 (Fig. 6c). The aspect ratio of the analyzed bubbles ranges from 1.02 (210_6 and 214_7) to 8.34 (223_3) (Fig. 6c). For the 0.5 mm^2 threshold, the largest 5,156 bubbles have aspect ratios between 1.022 (210_2) and 8.34 (223_3) (Fig. 6c) with a respective median and mean of 1.8 and 2.1, respectively. Mean aspect rations differ strongly between samples and decrease slightly with depth below 144 m (Fig. 6b). The distributions in Fig. 6c are right-skewed for all bubbles and bubbles greater than 0.5 mm^2. Fig. B1 displays histograms of aspect ratios for each bubble analyzed in the respective samples showing a similar distribution as the overview plot (Fig. 6c). Most bubbles show small aspect ratios and numbers decrease with increasing aspect ratio.

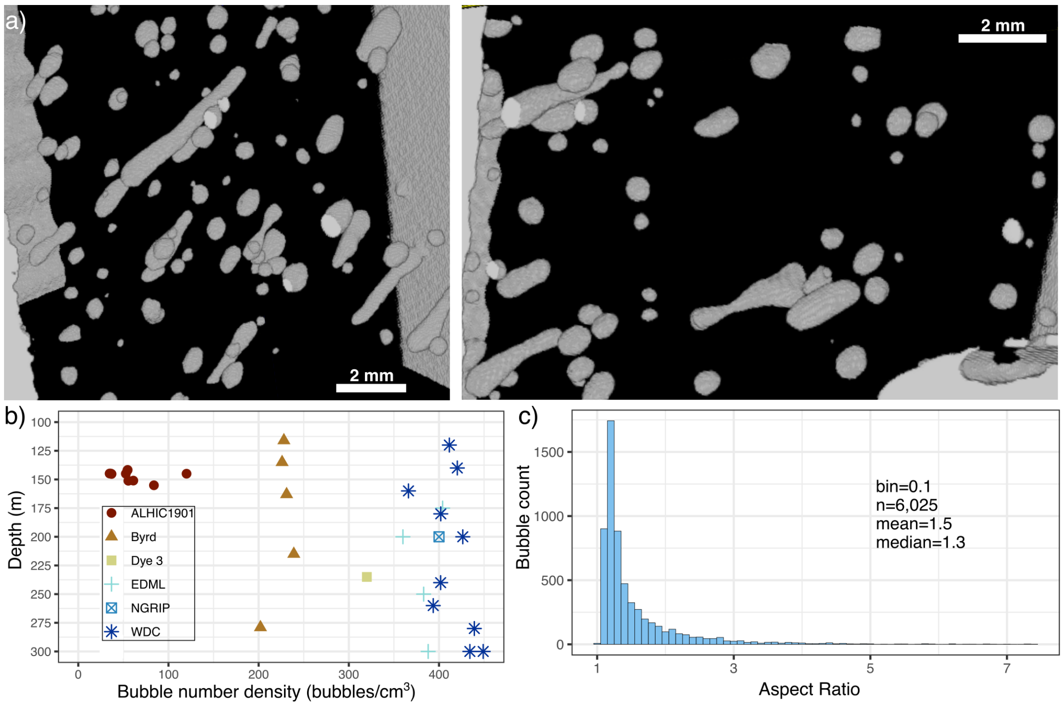

Figure 7. a) Reconstructed 3D bubbles from the AWI 3D CT. Cut bubbles are an artifact of the chosen plane of view. b) Bubble number density in ALHIC1901 compared to similar depths from the Byrd (Gow, 1968), Dye 3 (Shoji & Langway, 1985), EDML (Bendel et al., 2013), NGRIP (Kipfstuhl et al., 2001) and WAIS Divide Ice Core (WDC, R. Alley and Fegyveresi (2014)) ice cores. c) Histogram of aspect ratios for all analyzed 3D bubbles in 10 ALHIC1901 samples. For better visibility, we do not display the six values above 7.5.

3.4 3D Bubble Characteristics from CT Measurements

We analyzed a total of 6,030 3D bubbles across 10 samples (Fig. 7a). The analyzed sample volume and the number of bubbles within ranged from 5.81 to 17.98 cm^3 and 202 to 1299, respectively. Details can be found in Table C1. The bubble number density ranges from 34.7 (214_3) to 120 (214_5) bubbles per cm^3 and increases slightly with depth (Fig. 7b). The average is 59 bubbles per cm^3. Bubble number density can vary distinctly between close-by samples; for example, the two 214_5 samples display values of 52.7 and 120 bubbles per cm^3. Bubbles vary in volume from 0.0005 (214_4) to 1.0 mm^3 (214_3) with a mean and median of 0.08 and 0.04 mm^3, respectively. Aspect ratios range from 1.0 (228_4) to 14.2 (214_6) with a mean and median of 1.5 and 1.3, respectively (Fig. 7c). We display a representative selection of aspect ratio histograms for each analyzed bubble per sample in Fig. D1. Porosity of the analyzed areas ranges from 0.32 (228_4) to 0.55% (210_7).

4 Discussion

We here investigated the fabric, texture, and air-bubble properties at four depth regimes within the ALHIC1901 core, providing a first microstructural characterization of million-year-old AH blue ice. In the following, we identify simple shear as the dominant deformation regime, accompanied by dynamic recrystallization. These processes occur at all analyzed depths, with additional, strongly localized shear zones in the form of stripes of differently oriented crystals. In the following subsections, we will discuss these features in comparison with other ice cores and their potential impact on the climate record.

4.1 Fabric - Implications for Simple Shear Deformation and Ice Flow

The measured CPO patterns throughout all 4 depth regimes display broad single maxima, occasionally transforming into a double maxima vaguely resembling a tilted girdle CPO (Fig. 3). At our samples' depth of around 150 m (deepest 10% of ice column), one usually observes random CPOs in deep ice cores (Thorsteinsson et al., 1997; Fitzpatrick et al., 2014; Montagnat et al., 2014), even in dynamic regions such as fast-flowing ice streams (Stoll et al., 2025). However, despite its old age, ALHIC1901 is only limitedly comparable to these cores due to its short length. We explain the observed single maximum CPOs by the dominance of simple shear resulting in a rigid-body rotation of the grains, and thus, their c-axes (W. B. Kamb, 1959; B. Kamb, 1972; R. B. Alley, 1992; Llorens, Griera, Bons, Lebensohn, et al., 2016). The internal c-axis rotation is towards the greatest compressive stress direction, i.e., inclined at 45° to the shear plane, probably taking several hundreds to thousands of years. The observed double maxima CPOs agree with deformation experiments exposing ice to simple shear (e.g., Rigsby, 1960; B. Kamb, 1972; Duval, 1981; Bouchez & Duval, 1982; Paterson, 1994; Llorens, Griera, Bons, Roessiger, et al., 2016; Qi et al., 2019). The occasional vague tilted girdle CPO could indicate varying amounts of recrystallization or an additional horizontal extension component, as recently observed in the EastGRIP ice core from the Northeast Greenland Ice Stream (Stoll et al., 2025). Horizontal extension leads to c-axes rotating away from the axis of extension, which could increase highly localized shearing and therefore explain the infrequent occurrence of tilted girdles (Fig. 3). For the overall ice flow, we thus infer that deep ice at the ALHIC1901 site follows the surface ice flow (Fig. 8a), resulting in simple shear along the strongly tilted bedrock (Fig. 8b).

The large differences in the Woodcock parameter (Fig. 4b) and the respective CPOs (Fig. 3) of the deepest sample 228_4 indicate comparably strong differences in crystal orientation across a few vertical and horizontal centimeters. These differences could result in different rheologies and consequently highly localized shear zones on the centimeter-scale. Investigating this sample in more detail, using a variety of data sets, is ongoing work.

The observed dipping of the center of symmetry of the c-axes (13 to 38° from vertical, i.e., orthogonal basal planes dip 13 to 38° from the horizontal) likely represents the dip of the bedrock. This agrees well with 3D multitrack electrical conductivity measurements (ECM), which show layer dips (assumed to be parallel to bedrock) of 38° and 29°

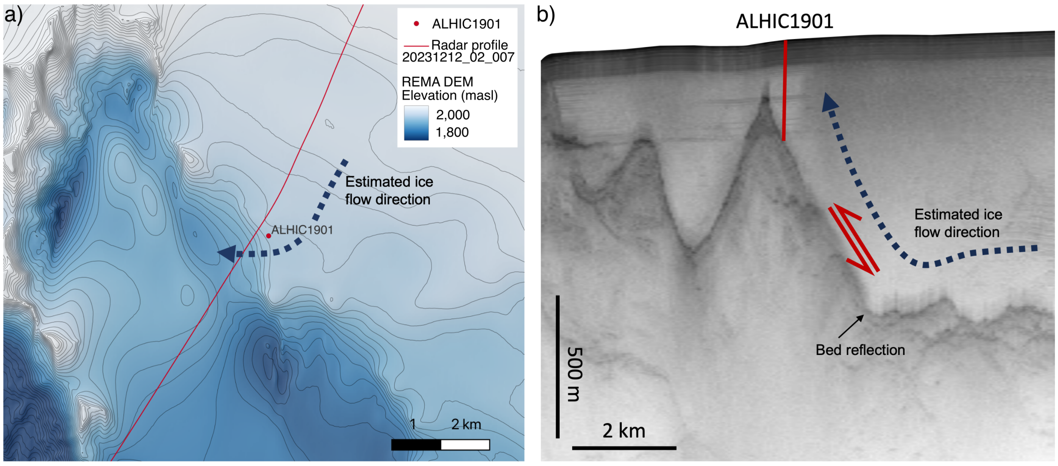

Figure 8. Estimated ice flow and deformation close to ALHIC1901. a) Radar profile close to ALHIC1901 displayed on the Reference Elevation Model of Antarctica (REMA, I. M. Howat et al. (2019); I. Howat et al. (2022)) Digital Elevation Model (DEM). b) Radar-derived bedrock topography (CReSIS, 2023) and ice flow direction with indicated simple shear deformation and bed reflection; note the vertical exaggeration.

from the horizontal for ALHIC1901 (155 and 157 m) and the nearby core ALHIC2201 (25-45 m), respectively (Kirkpatrick et al., 2025). Especially our deepest samples (155 m), display almost exactly the same dips (32°-37°) as the ECM data. This might be useful for future characterizations of the bedrock topography for e.g., ice flow modeling. However, synchronized measurements on the same samples are necessary to investigate this further.

4.2 Grain Size and Shape - Implications for Dynamic Recrystallization

The measured grain size is comparable to shallow samples from deep ice cores, such as EDML (Weikusat et al., 2017), GRIP (Thorsteinsson et al., 1997), or EastGRIP (Stoll et al., 2025). However, ALHIC1901 grains are very small, despite having had up to two million years to grow, compared to grains close to bedrock in deep ice cores, which can reach diameters of tens of centimeters or more. This is probably due to strong deformation and relatively cold ice temperatures. The ALHIC1901 borehole only shows a slight increase in temperature with depth, just exceeding -30°C in the deepest measurement (Fig. 1b). Due to the comparable thin ice column at the ALHIC1901 site, thermal insulation is weak, and close-to-bedrock ice does not warm contrary to deep ice core sites. This explains that ALHIC1901 grains close to bedrock are not much larger than grains from shallower depths, as often observed in other ice cores close to bedrock (e.g., Budd et al., 1976; Gow et al., 1997; Stoll et al., 2025). Our data show that time alone is not a dominant factor in grain growth, even though the largest grains are in the second-oldest sample, 214_5. This is probably different at locations chosen for the Oldest Ice quest (Fischer et al., 2013), which aim to retrieve continuous records, where very large grains are expected in the oldest ice.

The difference in mean grain size in sample 228_4 between vertical (3-4.8 mm^2) and horizontal sections (8.2 mm^2) indicates that grains are elongated perpendicular to the ice core axis. Grains in vertical sections also display straighter grain boundaries and a preferred orientation, likely parallel to the shear plane (Fig. 5c). This is consistent with the observed bubble aspect ratios, which show strong elongation in 2D and 3D. Analyzing several "volume sections" (containing vertical and horizontal sections for a quasi-3D analysis, as done by e.g., Hellmann et al. (2021)) are needed to provide more insights.

Strain energy drives the migration of grain boundaries, resulting in complex grain geometries, which we observed at all depths. High-angle grain boundaries migrate towards areas of higher density of stored strain energy and lattice defects, driving grain boundary migration (Kipfstuhl et al., 2006). These dislocation density differences between neighboring grains result in the observed grain boundary bulging features (Fig. 5c) (Weertman & Weertman, 1992; Humphreys & Hatherly, 2004; Weikusat et al., 2009). Nakaya (1958) showed that subgrain boundaries usually develop in regions of maximum stress/strain concentration. Strain localization on the sub-centimeter scale is probably rather the rule than the exception, but difficult to identify via microstructural analysis (Bons & Jessell, 1999). However, examples for strain localization are interactions between subgrain boundaries and grain boundaries. Migration recrystallization with nucleation and rotation recrystallization (also called polygonization) are the primary processes creating island grains (Urai et al., 1986; R. B. Alley, 1992), which we observed regularly (Fig. 5c). These nucleated islands form inside strongly distorted parent grains, which are characterized by networks of subgrain boundaries and dislocation walls (Faria et al. (2014) and references within). The regular occurrence of the three different subgrain boundary types (normal, parallel, zig-zag) indicates a high dislocation density resulting in the alignment of dislocations into walls (Weikusat et al., 2009). No depth-related trend in subgrain boundary occurrence or appearance was visible despite the large differences in sample age. Together with the grain shape information, we can conclude that dynamic recrystallization (rotation and migration recrystallization) is active at all analyzed depths.

4.3 Bubble Characteristics - Implications for Shearing and Paleoinformation Derived from Bubble Number Density

Bubbles in ice under little strain are usually (close to) sphere-shaped (Gow, 1968). However, bubble shapes change due to deformation of the surrounding ice and the prevailing ice flow. The bubble shape reflects the competing processes of ice deformation, causing elongation and surface-tension forces restoring the more efficient spherical shape (Hudleston, 1977). Therefore, bubble shape is an indicator of current, local deformation rates, but may also have memory of previous deformation regimes. The timescale of the memory is not well constrained but is likely hundreds to thousands of years, depending on strain rate, temperature, and other factors (R. B. Alley & Fitzpatrick, 1999). Bubbles are assumed to experience strain roughly 5/3 faster than the surrounding ice (R. B. Alley & Fitzpatrick, 1999). We are not aware of any laboratory experiments or observational data that confirm or refute this assumption. Unfortunately, only a few studies focus on the shape of bubbles in ice cores and their response to strain, limiting interpretation (R. B. Alley & Fitzpatrick, 1999; Ueltzhöffer et al., 2010; Drews et al., 2012; Bendel et al., 2013; J. M. Fegyveresi et al., 2019).

We analyzed the aspect ratio, i.e., elongation, of more than 19,600 bubbles in 2D (Fig. 6) and 6,000 bubbles in 3D (Fig. 7b). Both data sets show aspect ratio means of about 1.5 and maximum values above 7 while J. M. Fegyveresi et al. (2019) analyzed almost 4,000 bubbles in a WAIS Divide Ice Core (WDC) sample (580 m, ∼2252 yr) with maximum aspect ratios of 3.4. The agreement between the two data sets indicates that the means of the 2D data were not significantly biased by the single projection, and we note that work is ongoing to more fully characterize the relationship between 2D and 3D imaging of bubbles. The bubbles in ALHIC1901 are much more elongated than bubbles in most polar ice cores (e.g., Ueltzhöffer et al., 2010; Fitzpatrick et al., 2014; J. M. Fegyveresi et al., 2016, 2019), but resemble bubbles observed at distinct depths of the Taylor Dome core (Fig. 1c in R. B. Alley and Fitzpatrick (1999)). Analyses of bubbles in WDC show the evolution from the firn-ice transition (∼100 m) to clathrate transition (∼1600 m). Fitzpatrick et al. (2014); J. M. Fegyveresi et al. (2016) report a wide variety of bubble shapes below the firn-ice transition, an average aspect ratio of 1.2 at 400 m, and that bubbles become less elongated with depth until the bubble-free ice at ∼1600 m.

Smith (1975) proposed that, at large strains, bubbles are highly elongated and their rate of rotation and elongation will be similar to the surrounding ice, making them a passive strain marker. In simple shear, bubbles further tend towards parallelism with the shear plane (Hooke & Hudleston, 1978). The strongly elongated ALHIC1901 bubbles indicate that significant shearing has occurred for a sufficiently long time over the entire analyzed depth regime. This further supports our conclusion that the dominant deformation is simple shear.

The average 2D bubble size decreases with depth, even over the comparably small depth range of 14 m analyzed here. While the trend is consistent with previous studies (e.g., Gow, 1968; Fitzpatrick et al., 2014; J. M. Fegyveresi et al., 2016), the rate of decrease is much larger. The ALHIC1901 measurements are difficult to directly compare with deep ice core sites because of the much shallower ice thickness, such that our samples from ∼150 m depth are only ∼10 m above the bed.

The trend in aspect ratio with depth is less clear due to high variability across samples. Due to increasing pressure with depth, it is assumed that bubble elongation decreases with depth, as observed in WDC (Fitzpatrick et al., 2014; J. M. Fegyveresi et al., 2016). However, localized shearing zones might impact bubble elongation. Furthermore, mean aspect ratios per sample increase when applying the bubble size threshold of 0.5 mm, agreeing with observational and modeling studies (R. B. Alley & Fitzpatrick, 1999; J. M. Fegyveresi et al., 2019). Nakawo and Wakahama (1981) showed that bubbles can also form from cracks in ice during compressional deformation. The ALHIC1901 core contains several cracks, and we cannot rule out that some bubbles developed from these. However, the widespread occurrence of strongly elongated bubbles in intact samples and the visual observation (in the field and during core processing) of similarly shaped bubbles in other AH cores indicate a deformation-related origin for these features. In addition, there is uncertainty about whether the analyzed bubbles are resurfaced clathrates, a topic so far (to our knowledge) unexplored. However, recent work on the EDML core showed that the clathrate aspect ratio can also change due to deformation (Painer et al., 2025).

The much larger bubble size in ALHIC1901 compared to interior deep ice cores could be due to either the firn densification process, or coalescence of bubbles either through deformation or returning from clathrate form. The paleoclimate importance of this question is addressed in Section 4.5. The large bubbles may be due to the unusual densification on the Allan Hills. Densification of polar firn is mainly driven by accumulation rate and temperature, which is recorded in the bubble number density, enabling the reconstruction of paleotemperature or paleo-accumulation if one of these parameters is known (e.g., Spencer et al., 2006; J. Fegyveresi et al., 2011). According to Gow (1968), larger ice crystals at pore close-off result in a small number of large bubbles, and the bubble number density preserves firnification conditions longer than the ice crystals, which are affected by processes, such as recrystallisation and growth. Although the AH firn densification is not well constrained, the very low accumulation rates potentially allow very large grain development as the firn closes off at a shallow depth (i.e., it doesn't get buried by subsequent accumulation) and is exposed to strong temperature and vapor gradients. Further, the firn may experience periods of both accumulation and ablation (due to temporal and spatial variability), which could produce large bubbles. On the other hand, the ice-flow history of the ALHIC1901 ice is similarly poorly constrained. The ice parcels may have been much deeper in the ice sheet; ice thicknesses are >1200 m within 10 km (Kehrl et al., 2018), or the ice could have originated in the interior of East Antarctica at depths greater than 3000 m. In either case, some or all of the bubbles may have transitioned to clathrates. Therefore, we cannot rule out that the large bubbles result from the coalescence of air transitioning back to bubbles from clathrates.

4.4 Small-scale Folding Impacts the ALHIC1901 Stratigraphy

Polar ice is monomineralic and layers in an ice sheet thus have no critical competence differences, i.e., varying resistance against deformation. However, differences in rheological properties can occur due to the complex, and still not fully understood, interplay between fabric, grain size and impurity content (e.g., R. B. Alley et al., 1986; Paterson, 1991; Stoll et al., 2021). As no distinct differences in grains size were observed and no microstructural impurity localization data is available, we here focus on the impact of fabric, particularly the observed stripes of differently oriented crystals, to explain the observed age reversals in ALHIC1901. Future studies using, for example, laser ablation inductively coupled plasma mass spectrometry 2D imaging and Raman spectroscopy could investigate the impurity content and localization to explore post-depositional processes in million-year-old ice (e.g., Stoll, Bohleber, et al., 2023).

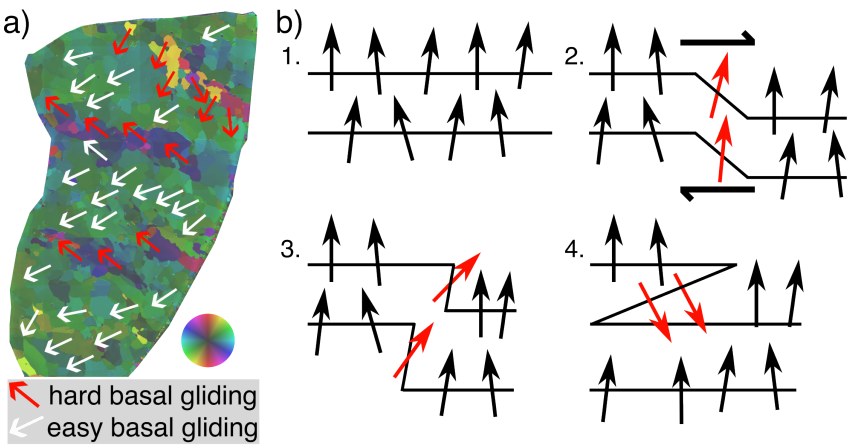

Figure 9. Sketch displaying a) simplified c-axes orientations in the ice matrix and the described stripes by the example of 210_4 and b) a possible evolution of z-folds in dextral shear (after R. B. Alley et al. (1997), not quantitatively accurate). C-axes are indicated by arrows and stratigraphic layers by lines. Red arrows represent c-axes in the stripes from a).

Similar to our observations, stripes of differently oriented crystals were observed in the deep ice cores GISP2, GRIP and NEEM (R. B. Alley et al., 1997; Thorsteinsson et al., 1997; Jansen et al., 2016). In GISP2, stripes are often found within stratigraphic disturbances visible in polished samples (R. B. Alley et al., 1997). Thorsteinsson et al. (1997) observed stripes only at a few selected depths containing a strong single maximum CPO, especially in disturbed sections of GRIP. In NEEM, Jansen et al. (2016) observed, and successfully modeled, bands differing in inclination, which were interpreted as different generations of tilted-lattice bands (kink bands). Since their formation, older bands have experienced more shear strain leading to a shift in c-axes orientations. We observed similar occurrences, e.g., in the pronounced bands in 210_4 and 211_2.

We interpret the stripes in ALHIC1901 as indications of small-scale folding via kink and z-folds as observed in GISP2 (R. B. Alley et al., 1997), EDML (Faria et al., 2010), NEEM (Jansen et al., 2016), and other geological settings (e.g., Sitter, 1964; Anderson, 1964; Dewey, 1965; Anderson, 1968). The observed stripes usually contain crystals oriented 10 to 60° from the vertical, while the centers of symmetry, i.e., c-axes of the matrix, dip with 13 to 38°. Crystal stripes are thus softened for vertical compression and hardened for basal gliding compared to crystals with a more vertical orientation (Fig. 9a). The differently oriented c-axes in stripes make them more robust to simple shear (parallel to the bed) and less robust to layer thinning than the surrounding ice. Thus, small-scale ice flow around these stripes will differ, potentially resulting in kink folds containing smaller z-folds (Fig. 9b) and potentially even duplex structures. Kink folds are asymmetric folds with straight limbs and sharp (mobile or fixed) hinges, which can develop through simple shear. They were observed in ice cores (R. B. Alley et al., 1997; Faria et al., 2010; Jansen et al., 2016) and were recently discussed for ice sheets at the centimeter-to-kilometer scale (Bons et al., 2025). Between the two kink planes, the kink band contains a zone of highly localized shear strain (shear zone). Kink banding is assumed to be restricted to crystals with c-axes oriented vertically to the shortening direction in simple shear(C. J. L. Wilson & Zhang, 1994). Therefore, folding and flow disturbances are likely to create strongly localized shear zones, thereby altering the initial ice-core stratigraphy. This agrees with recent 3D multitrack ECM showing strong layer dipping only a few meters away from the ALHIC1901 site (Kirkpatrick et al., 2025).

In this study, we were limited to thin-section-sized snapshots of a few depths. These partly explain the complex depth-age relationship in ALHIC1901, which is characterized by simple shear deformation and several centimeter-scale folds. However, it remains challenging to assess potential folding over scales of tens of meters. An extended study investigating several meters continuously is the next step to address if, and to what extent, small-scale folding has impacted the mesoscale. Additional visual stratigraphy (e.g., Svensson et al., 2005; Stoll, Westhoff, et al., 2023), 3D ECM (Fudge et al., 2016; Kirkpatrick et al., 2025), and hyperspectral imaging (e.g., Garzonio et al., 2018; McDowell et al., 2024) data could help to dissect age inversions over dozens of meters and to, e.g., estimate their size, as done in EDML, where decimeter-sized z-folds were found (Faria et al., 2010). Additionally, recording or reconstructing the core's original orientation, i.e., the azimuth, would be valuable for interpreting microstructural data in a larger kinematic context.

4.5 Implications for the ALHIC1901 Palaeorecord

The observed small-scale folds imply that mixing of different layers is occurring in the deep ALHIC1901 ice, at least at the centimeter scale. These folds, however, are at too small of a scale to explain the age reversals observed with the $^{40}Ar_{atm}$ dating. In particular, the vertical sections in 228_4 (Fig. 3) do not exhibit either grain size or fabric differences across the distinct layering imaged by 3D ECM on this section. The small-scale folds observed here are similar to those in GISP2 (R. B. Alley et al., 1997); however, their interpretation is unlikely to be the same. In GISP2, the folds occurred hundreds of meters above the bed, where disruptions to the stratigraphic record grew with depth. In ALHIC1901, the small-scale folds are only meters above the bed, and the stratigraphic layering above is disturbed. Thus, it is unclear if the small—scale folds are part of the mechanism disrupting the stratigraphic layering. Kirkpatrick et al. (2025) found consistent layering in the upper ∼50 m of the nearby ALHIC2201 core, despite age reversals through the same depth range; they thus suggested that the stratigraphic discontinuity may reflect recumbent folds. Without measurements of ice crystal properties at these depths, it is unclear whether such recumbent folding is ongoing or the result of processes upstream.

The bubble number density in ALHIC1901 is extremely low compared to other ice cores from Antarctica and Greenland (Fig. 7a). This raised an important question regarding the large bubbles: do they result from a low-accumulation firn densification process?; from the process of clathrates returning to bubbles as the pressure decreases due to the thinner ice?; or because of large amounts of time for coalescence of bubbles to outweigh any bubble splitting? The very low bubble number densities across our samples may indicate that the originally preserved bubbles were altered, potentially affecting the effective smoothing of the paleorecord. We assume that smaller bubbles were pushed together, coalescing into fewer, but larger bubbles - a likely consequence of the currently observed simple shear and folding. Currently, we cannot estimate how long this has been going on. However, these findings imply that the gas record in the bubbles could be mixed. Another explanation could be specific conditions during bubble formation in the firn, resulting in originally very large bubbles.

The lack of full-depth microstructural measurements in the AH is a significant limitation in interpreting our samples from near the bed. The AH is a unique glaciological environment, so inference from deep, interior ice-core sites may not be applicable. Our work highlights the ongoing challenge of determining the best approach for cutting, analyzing, and interpreting ALHIC1901 and other AH ice cores. Dedicated microstructural measurements on continuous sections, together with new developments in stratigraphy reconstruction (e.g., Kirkpatrick et al., 2025), will enable a better constraint on the alteration of the palaeorecord.

5 Conclusions

Here, we used a variety of methods to derive the first characterization of crystal-preferred orientation, grain size and shape, and bubble characteristics in the ALHIC1901 ice core, which extends back 2 million years from the Allan Hills Blue Ice region, Antarctica. We identified simple shear as the main deformation resulting in strongly elongated air bubbles and single to double maxima CPOs. Stripes of crystals oriented differently to the ice matrix indicate that z-folds and kink bands are common, leading to a disturbed depth-age relationship. Irregular grain shapes and microstructural features further indicate dynamic recrystallization at all analyzed depths. The very low bubble number densities relative to other ice cores indicate bubble coalescence, which assumedly also altered the air bubble content. The limited number of analyzed samples makes it challenging to transfer these results to the entire ALHIC1901 core and the larger Allan Hills area. Thus, more systematic microstructural studies on other Allan Hills cores are needed to better understand the ice deformation and dynamics and, therefore, the preserved climate record.

Open Research Section

Author contribution

Conceptualization: Nicolas Stoll, T.J. Fudge.
Data curation: Nicolas Stoll, Johannes Freitag, John-Morgan Manos, Valens Hishamunda.
Formal analysis: Nicolas Stoll, Johannes Freitag, Marguerite Shaya, John-Morgan Manos.
Funding acquisition: Nicolas Stoll, T.J. Fudge, Ed Brook, John Higgins, Bradley Paul Lipovsky.
Investigation: Nicolas Stoll, T.J. Fudge, Johannes Freitag, Liam Kirkpatrick, Marguerite Shaya, Valens Hishamunda, Sarah Shackleton.
Methodology: Nicolas Stoll, T.J. Fudge, John Fegyveresi, Marguerite Shaya, Johannes Freitag.
Supervision: T.J. Fudge, Ed Brook, John Higgins, Bradley Paul Lipovsky.
Writing – original draft: Nicolas Stoll.
Writing – review & editing: Nicolas Stoll, T.J. Fudge, Liam Kirkpatrick, Marguerite Shaya, Johannes Freitag, Ilka Weikusat, Daniela Jansen, John Fegyveresi.

Data availability

- Fabric derived by G50 Fabric Analyzer: Stoll, N. (2026) "Allan Hills ALHIC1901 ice core fabric data" U.S. Antarctic Program (USAP) Data Center. doi: https://doi.org/10.15784/602011.

- 2D bubble data derived by image analysis: Stoll, N., & Fudge, T. J. (2026) ”Allan Hills ALHIC1901 ice core 2D bubble parameters” U.S. Antarctic Program (USAP) Data Center. doi: https://doi.org/10.15784/602010.
- 3D bubble data derived by 3D CT: Stoll, N., & Freitag, J. (2026) ”Allan Hills ALHIC1901 ice core 3D bubble parameters” U.S. Antarctic Program (USAP) Data Center. doi: https://doi.org/10.15784/602009.
- Texture derived by LASM: Stoll, N. (2026) ”Allan Hills ALHIC1901 ice core texture images” U.S. Antarctic Program (USAP) Data Center. doi: https://doi.org/10.15784/602018.
- Bore hole temperature: `https://github.com/johnmorganmanos/AH_temp_paper/tree/main/Borehole_Temps`

Conflict of interest

The authors declare that there is no conflict of interest.

Acknowledgments

This work was supported by the U.S. National Science Foundation Center for Oldest Ice Exploration (NSF COLDEX), an NSF Science and Technology Center (NSF 2019719). We thank the U.S. National Science Foundation Ice Core Facility (NSF-2041950) for ice core sampling assistance and curation. We thank the NSF Office of Polar Programs, the NSF Office of Integrative Activities, and Oregon State University for financial and infrastructure support, and the NSF Antarctic Infrastructure and Logistics Program, and the Antarctic Support Contractor for logistical support. We thank the NSF Ice Drilling Program for support activities through NSF Continuing Grant 2318480, the field team retrieving ALHIC1901 and all NSF COLDEX members contributing to the ice core processing. Further, we thank Sonja Wahl for assistance with the sample transport and Denise Diekstall and Hennig Ullrich for preparing the AWI ice laboratories. Nicolas Stoll was funded by NSF Award 2149518 and a postdoc fellowship (*RESTORATION*) from the German Academic Exchange Service (DAAD). Nicolas Stoll also acknowledges funding from the European Union's Horizon 2020 research and innovation program under the Marie Skłodowska-Curie grant agreement no. 101146092. We acknowledge the use of data and/or data products from CReSIS generated with support from the University of Kansas, NSF grant ANT-0424589, and NASA Operation IceBridge grant NNX16AH54G. Geospatial support for this work provided by the Polar Geospatial Center under NSF-OPP awards 1043681, 1559691, and 2129685. DEMs provided by the Byrd Polar and Climate Research Center and the Polar Geospatial Center under NSF-OPP awards 1043681, 1542736, 1543501, 1559691, 1810976, and 2129685.

References

Alley, R., & Fegyveresi, J. M. (2014). *Bubble Number-density Data and Modeled Paleoclimates.* U.S. Antarctic Program Data Center (USAP-DC), via National Snow and Ice Data Center (NSIDC). Retrieved 2025-11-10, from `http://www.usap-dc.org/view/dataset/609538` doi: 10.7265/N5JW8BTJ

Alley, R. B. (1992). Flow-law hypotheses for ice-sheet modeling. *Journal of Glaciology*, *38*(129), 245 – 256. doi: https://doi.org/10.3189/S0022143000003658

Alley, R. B., & Fitzpatrick, J. J. (1999). Conditions for bubble elongation in cold ice-sheet ice. *Journal of Glaciology*, *45*(149), 147–153. doi: 10.1017/S0022143000003129

Alley, R. B., Gow, A. J., & Meese, D. A. (1995, January). Mapping c-axis fabrics to study physical processes in ice. *Journal of Glaciology*, *41*(137), 197–203. Retrieved 2024-05-02, from `https://www.cambridge.org/core/journals/journal-of-glaciology/article/mapping-caxis-fabrics-to-study`

-physical-processes-in-ice/A53E03C68B23749F9EECFFAF1813DBC2 doi: 10.3189/S0022143000017895

Alley, R. B., Gow, A. J., Meese, D. A., Fitzpatrick, J. J., Waddington, E. D., & Bolzan, J. F. (1997). Grain-scale processes, folding, and stratigraphic disturbance in the GISP2 ice core. *Journal of Geophysical Research: Oceans*, *102*(C12), 26819–26830. Retrieved 2025-08-04, from https://onlinelibrary.wiley.com/doi/abs/10.1029/96JC03836 doi: 10.1029/96JC03836

Alley, R. B., Perepezko, J. H., & Bentley, C. R. (1986). Grain Growth in Polar Ice: II. Application. *Journal of Glaciology*, *32*(112), 425–433. doi: 10.1017/s0022143000012132

Anderson, T. B. (1964, April). Kink-Bands and Related Geological Structures. *Nature*, *202*(4929), 272–274. Retrieved 2025-08-07, from https://www.nature.com/articles/202272a0 doi: 10.1038/202272a0

Anderson, T. B. (1968). The geometry of natural ortho-rhombic systems of kink bands. *Geol. surv. Canada Paper*, *68*, 200–225. Retrieved 2025-08-07, from https://cir.nii.ac.jp/crid/1571980074389276032

Bendel, V., Ueltzhöffer, K. J., Freitag, J., Kipfstuhl, S., Kuhs, W. F., Garbe, C. S., & Faria, S. H. (2013). High-resolution variations in size, number and arrangement of air bubbles in the EPICA DML (Antarctica) ice core. *Journal of Glaciology*, *59*(217), 972–980. Retrieved 2024-09-17, from https://www.cambridge.org/core/product/identifier/S0022143000202955/type/journal_article doi: 10.3189/2013jog12j245

Bender, M. L., Barnett, B., Dreyfus, G., Jouzel, J., & Porcelli, D. (2008, June). The contemporary degassing rate of^{40} Ar from the solid Earth. *Proceedings of the National Academy of Sciences*, *105*(24), 8232–8237. Retrieved 2025-11-13, from https://pnas.org/doi/full/10.1073/pnas.0711679105 doi: 10.1073/pnas.0711679105

Binder, T., Garbe, C., Wagenbach, D., Freitag, J., & Kipfstuhl, S. (2013). Extraction and parametrization of grain boundary networks in glacier ice, using a dedicated method of automatic image analysis. *Journal of Microscopy*, *250*(2), 130–141. Retrieved 2024-03-18, from https://onlinelibrary.wiley.com/doi/abs/10.1111/jmi.12029 doi: 10.1111/jmi.12029

Bintanja, R. (1999). On the glaciological, meteorological, and climatological significance of Antarctic blue ice areas. *Reviews of Geophysics*, *37*(3), 337–359. Retrieved 2024-11-22, from https://onlinelibrary.wiley.com/doi/abs/10.1029/1999RG900007 (_eprint: https://onlinelibrary.wiley.com/doi/pdf/10.1029/1999RG900007) doi: 10.1029/1999RG900007

Bons, P. D., Hu, Y., Llorens, M.-G., Franke, S., Stoll, N., Weikusat, I., … Zhang, Y. (2025, October). Folding due to anisotropy in ice, from drill-core-scale cloudy bands to km-scale internal reflection horizons. *The Cryosphere*, *19*(10), 5095–5109. Retrieved 2025-11-14, from https://tc.copernicus.org/articles/19/5095/2025/ doi: 10.5194/tc-19-5095-2025

Bons, P. D., & Jessell, M. W. (1999, March). Micro-shear zones in experimentally deformed octachloropropane. *Journal of Structural Geology*, *21*(3), 323–334. Retrieved 2022-11-25, from https://www.sciencedirect.com/science/article/pii/S019181419890116X doi: 10.1016/S0191-8141(98)90116-X

Bouchez, J. L., & Duval, P. (1982). The Fabric of Polycrystalline Ice Deformed in Simple Shear: Experiments in Torsion, Natural Deformation and Geometrical Interpretation. *Textures and Microstructures*, *5*(C), 171–190.

Budd, W., Young, N., & Austin, C. (1976). Measured and Computed Temperature Distributions in the Law Dome Ice Cap, Antarctica. *Journal of Glaciology*, *16*(74), 99–110. Retrieved 2025-11-14, from https://www.cambridge.org/core/product/identifier/S0022143000031452/type/journal_article doi:

10.3189/S0022143000031452

CReSIS. (2023). *Radar profile ID:20231212_02_007* [CReSIS Radar Depth Sounder Data, Lawrence, Kansas, USA]. Digital Media. Retrieved from http://data.cresis.ku.edu/ doi: CReSISRadarDepthSounderData ,Lawrence,Kansas,USA

Dewey, J. F. (1965, April). Nature and origin of kink-bands. *Tectonophysics*, *1*(6), 459–494. Retrieved 2025-08-07, from https://www.sciencedirect.com/science/article/pii/0040195165900193 doi: 10.1016/0040-1951(65)90019-3

Dome Fuji Ice Core Project Members:, Kawamura, K., Abe-Ouchi, A., Motoyama, H., Ageta, Y., Aoki, S., ... Yoshimoto, T. (2017, February). State dependence of climatic instability over the past 720,000 years from Antarctic ice cores and climate modeling. *Science Advances*, *3*(2), e1600446. Retrieved 2024-11-15, from https://www.science.org/doi/10.1126/sciadv.1600446 doi: 10.1126/sciadv.1600446

Drews, R., Eisen, O., Steinhage, D., Weikusat, I., Kipfstuhl, S., & Wilhelms, F. (2012). Potential mechanisms for anisotropy in ice-penetrating radar data. *Journal of Glaciology*, *58*(209), 613–624. doi: 10.3189/2012JoG11J114

Duval, P. (1981). Creep and Fabrics of Polycrystalline Ice Under Shear and Compression. *Journal of Glaciology*, *27*(95), 129–140. doi: 10.3189/s002214300001128x

Eichler, J. (2013). *C-axis analysis of the NEEM ice core: an approach based on digital image processing* (Unpublished doctoral dissertation). Freie Universität Berlin, Berlin. (Issue: April)

EPICA Community Members. (2004). Eight glacial cycles from an Antarctic ice core EPICA community members. *Nature*, *429*(6992), 623–628. (ISBN: 0028-0836)

Faria, S. H., Freitag, J., & Kipfstuhl, S. (2010). Polar ice structure and the integrity of ice-core paleoclimate records. *Quaternary Science Reviews*, *29*(1-2), 338–351. doi: 10.1016/j.quascirev.2009.10.016

Faria, S. H., Weikusat, I., & Azuma, N. (2014, April). The microstructure of polar ice. Part II: State of the art. *Journal of Structural Geology*, *61*, 21–49. Retrieved 2025-04-02, from https://www.sciencedirect.com/science/article/pii/S0191814113002009 doi: 10.1016/j.jsg.2013.11.003

Fegyveresi, J., Alley, R., Spencer, M., Fitzpatrick, J., Steig, E., White, J., ... Taylor, K. (2011). Late-Holocene climate evolution at the WAIS Divide site, West Antarctica: bubble number-density estimates. *Journal of Glaciology*, *57*(204), 629–638. Retrieved 2025-11-13, from https://www.cambridge.org/core/product/identifier/S0022143000204139/type/journal_article doi: 10.3189/002214311797409677

Fegyveresi, J. M., Alley, R. B., Fitzpatrick, J. J., Cuffey, K. M., McConnell, J. R., Voigt, D. E., ... Stevens, N. T. (2016, March). Five millennia of surface temperatures and ice core bubble characteristics from the WAIS Divide deep core, West Antarctica. *Paleoceanography*, *31*(3), 416–433. Retrieved 2024-07-22, from https://agupubs.onlinelibrary.wiley.com/doi/10.1002/2015PA002851 doi: 10.1002/2015PA002851

Fegyveresi, J. M., Alley, R. B., Voigt, D. E., Fitzpatrick, J. J., & Wilen, L. A. (2019). Instruments and methods: A case study of ice core bubbles as strain indicators. *Annals of Glaciology*, *60*(78), 8–19. doi: 10.1017/aog.2018.23

Fischer, H., Severinghaus, J., Brook, E., Wolff, E., Albert, M., Alemany, O., ... Wilhelms, F. (2013). Where to find 1.5 million yr old ice for the IPICS "Oldest-Ice" ice core. *Climate of the Past*, *9*(6), 2489–2505. (ISBN: 1814-9332) doi: 10.5194/cp-9-2489-2013

Fitzpatrick, J. J., Voigt, D. E., Fegyveresi, J. M., Stevens, N. T., Spencer, M. K., Cole-Dai, J., ... Mcconnell, J. R. (2014, July). Physical properties of the WAIS Divide ice core. *Journal of Glaciology*, *60*(224), 1181–1198. doi:

10.3189/2014JoG14J100
Freitag, J., Kipfstuhl, S., & Laepple, T. (2013). Core-scale radioscopic imaging: a new method reveals density–calcium link in Antarctic firn. *Journal of Glaciology*, *59*(218), 1009–1014. Retrieved 2025-11-12, from https://www.cambridge.org/core/product/identifier/S0022143000203729/type/journal_article doi: 10.3189/2013JoG13J028
Fudge, T. J., Taylor, K. C., Waddington, E. D., Fitzpatrick, J. J., & Conway, H. (2016, July). Electrical stratigraphy of the WAIS Divide ice core: Identification of centimeter-scale irregular layering. *Journal of Geophysical Research: Earth Surface*, *121*(7), 1218–1229. Retrieved from http://doi.wiley.com/10.1002/2016JF003845 doi: 10.1002/2016JF003845
Garzonio, R., Di Mauro, B., Cogliati, S., Rossini, M., Panigada, C., Delmonte, B., ... Colombo, R. (2018, November). A novel hyperspectral system for high resolution imaging of ice cores: Application to light-absorbing impurities and ice structure. *Cold Regions Science and Technology*, *155*, 47–57. Retrieved 2025-11-14, from https://www.sciencedirect.com/science/article/pii/S0165232X17305797 doi: 10.1016/j.coldregions.2018.07.005
Gow, A. J. (1968, January). Bubbles and Bubble Pressures in Antarctic Glacier Ice. *Journal of Glaciology*, *7*(50), 167–182. Retrieved 2025-08-06, from https://www.cambridge.org/core/journals/journal-of-glaciology/article/bubbles-and-bubble-pressures-in-antarctic-glacier-ice/C8CB03F5D01BDA8C9D203B8BEDFC8FC4 doi: 10.3189/S0022143000030975
Gow, A. J., Meese, D. A., Alley, R. B., Fitzpatrick, J. J., Anandakrishnan, S., Woods, G. A., & Elder, B. C. (1997). Physical and structural properties of the Greenland Ice Sheet Project 2 ice core: A review. *Journal of Geophysical Research: Oceans*, *102*(C12), 26559–26575. Retrieved 2025-08-05, from https://onlinelibrary.wiley.com/doi/abs/10.1029/97JC00165 doi: 10.1029/97JC00165
Hellmann, S., Kerch, J., Weikusat, I., Bauder, A., Grab, M., Jouvet, G., ... Maurer, H. (2021, February). Crystallographic analysis of temperate ice on Rhonegletscher, Swiss Alps. *The Cryosphere*, *15*(2), 677–694. Retrieved 2024-01-12, from https://tc.copernicus.org/articles/15/677/2021/ doi: 10.5194/tc-15-677-2021
Higgins, J. A., Kurbatov, A. V., Spaulding, N. E., Brook, E., Introne, D. S., Chimiak, L. M., ... Bender, M. L. (2015, June). Atmospheric composition 1 million years ago from blue ice in the Allan Hills, Antarctica. *Proceedings of the National Academy of Sciences*, *112*(22), 6887–6891. Retrieved 2024-08-02, from https://www.pnas.org/doi/full/10.1073/pnas.1420232112 doi: 10.1073/pnas.1420232112
Hooke, R. L., & Hudleston, P. J. (1978, January). Origin of Foliation in Glaciers. *Journal of Glaciology*, *20*(83), 285–299. Retrieved 2025-08-06, from https://www.cambridge.org/core/journals/journal-of-glaciology/article/origin-of-foliation-in-glaciers/902E4CEE1F85585468203B6035EDE3DD doi: 10.3189/S0022143000013848
Howat, I., Porter, C., Noh, M.-J., Husby, E., Khuvis, S., Danish, E., ... Polar Geospatial Center (2022, October). *The Reference Elevation Model of Antarctica - Mosaics, Version 2.* Harvard Dataverse. Retrieved 2025-12-16, from https://dataverse.harvard.edu/citation?persistentId=doi:10.7910/DVN/X7NDNY doi: https://doi.org/10.7910/DVN/EBW8UC
Howat, I. M., Porter, C., Smith, B. E., Noh, M.-J., & Morin, P. (2019, February). The Reference Elevation Model of Antarctica. *The Cryosphere*, *13*(2), 665–674. Retrieved 2026-01-19, from https://tc.copernicus.org/articles/13/665/2019/ doi: 10.5194/tc-13-665-2019
Hudleston, P. J. (1977). Progressive Deformation and Development of Fabric Across Zones of Shear in Glacial Ice. In S. K. Saxena, S. Bhattacharji, H. Annersten,

& O. Stephansson (Eds.), *Energetics of Geological Processes: Hans Ramberg on his 60th birthday* (pp. 121–150). Berlin, Heidelberg: Springer. Retrieved 2025-08-04, from https://doi.org/10.1007/978-3-642-86574-9_7 doi: 10.1007/978-3-642-86574-9_7

Humphreys, F., & Hatherly, M. (2004). *Recrystallization and Related Annealing Phenomena.* Elsevier. (Publication Title: Recrystallization and Related Annealing Phenomena: Second Edition) doi: 10.1016/B978-0-08-044164-1.X5000-2

Jansen, D., Llorens, M.-G., Westhoff, J., Steinbach, F., Kipfstuhl, S., Bons, P. D., ... Weikusat, I. (2016, February). Small-scale disturbances in the stratigraphy of the NEEM ice core: observations and numerical model simulations. *The Cryosphere*, *10*(1), 359–370. Retrieved from https://tc.copernicus.org/articles/10/359/2016/ doi: 10.5194/tc-10-359-2016

Kamb, B. (1972). Experimental Recrystallization of Ice Under Stress. *Flow and Fracture of Rocks, American Geophysical Union Geophysical Monograph*, *16*, 211–241. doi: 10.1029/GM016p0211

Kamb, W. B. (1959). Ice petrofabric observations from Blue Glacier, Washington, in relation to theory and experiment. *Journal of Geophysical Research (1896-1977)*, *64*(11), 1891–1909. Retrieved 2024-01-15, from https://onlinelibrary.wiley.com/doi/abs/10.1029/JZ064i011p01891 doi: 10.1029/JZ064i011p01891

Kehrl, L., Conway, H., Holschuh, N., Campbell, S., Kurbatov, A. V., & Spaulding, N. E. (2018). Evaluating the Duration and Continuity of Potential Climate Records From the Allan Hills Blue Ice Area, East Antarctica. *Geophysical Research Letters*, *45*(9), 4096–4104. Retrieved 2024-08-02, from https://onlinelibrary.wiley.com/doi/abs/10.1029/2018GL077511 doi: 10.1029/2018GL077511

Kipfstuhl, S., Hamann, I., Lambrecht, A., Freitag, J., Faria, H., Sergio, Grigoriev, D., & Azuma, N. (2006). Microstructure mapping: a new method for imaging deformation-induced microstructural features of ice on the grain scale. *Journal of Glaciology*, *52*(178), 398–406.

Kipfstuhl, S., Pauer, F., Kuhs, W. F., & Shoji, H. (2001). Air bubbles and Clathrate hydrates in the transition zone of the NGRIP Deep Ice Core. *Geophysical Research Letters*, *28*(4), 591–594. Retrieved 2025-07-04, from https://onlinelibrary.wiley.com/doi/abs/10.1029/1999GL006094 doi: 10.1029/1999GL006094

Kirkpatrick, L. R., Carter, A. J., Marks-Peterson, J., Shackleton, S., & Fudge, T. (2025). Three-dimensional multitrack electrical conductivity method for interpretation of complex ice core stratigraphy. *Journal of Glaciology*, *71*, e105. Retrieved 2025-10-24, from https://www.cambridge.org/core/product/identifier/S0022143025100816/type/journal_article doi: 10.1017/jog.2025.10081

Krischke, A., Oechsner, U., & Kipfstuhl, S. (2015). Rapid Microstructure Analysis of Polar Ice Cores. *Optik & Photonik*, *10*(2), 32–35. Retrieved from http://doi.wiley.com/10.1002/opph.201500016 doi: 10.1002/opph.201500016

Llorens, M.-G., Griera, A., Bons, P. D., Lebensohn, R. A., Evans, L. A., Jansen, D., & Weikusat, I. (2016, September). Full-field predictions of ice dynamic recrystallisation under simple shear conditions. *Earth and Planetary Science Letters*, *450*, 233–242. Retrieved 2024-03-15, from https://www.sciencedirect.com/science/article/pii/S0012821X16303326 doi: 10.1016/j.epsl.2016.06.045

Llorens, M. G., Griera, A., Bons, P. D., Roessiger, J., Lebensohn, R., Evans, L., & Weikusat, I. (2016). Dynamic recrystallisation of ice aggregates during co-axial viscoplastic deformation: A numerical approach. *Journal of Glaciology*, *62*(232), 359–377. doi: 10.1017/jog.2016.28

Lüthi, D., Le Floch, M., Bereiter, B., Blunier, T., Barnola, J. M., Siegenthaler, U., . . . Stocker, T. F. (2008). High-resolution carbon dioxide concentration record 650,000-800,000 years before present. *Nature*, *453*(7193), 379–382. doi: 10.1038/nature06949

McDowell, I. E., Keegan, K. M., Skiles, S. M., Donahue, C. P., Osterberg, E. C., Hawley, R. L., & Marshall, H.-P. (2024, April). A cold laboratory hyperspectral imaging system to map grain size and ice layer distributions in firn cores. *The Cryosphere*, *18*(4), 1925–1946. Retrieved 2025-11-14, from `https://tc.copernicus.org/articles/18/1925/2024/` doi: 10.5194/tc-18-1925-2024

Montagnat, M., Azuma, N., Dahl-Jensen, D., Eichler, J., Fujita, S., Gillet-Chaulet, F., . . . Weikusat, I. (2014). Fabric along the NEEM ice core, Greenland, and its comparison with GRIP and NGRIP ice cores. *Cryosphere*, *8*(4), 1129–1138. doi: 10.5194/tc-8-1129-2014

Nakawo, M., & Wakahama, G. (1981, January). Preliminary Experiments on the Formation of Elongated Air Bubbles in Glacier Ice by Stress. *Journal of Glaciology*, *27*(95), 141–146. Retrieved 2025-08-06, from `https://www.cambridge.org/core/journals/journal-of-glaciology/article/preliminary-experiments-on-the-formation-of-elongated-air-bubbles-in-glacier-ice-by-stress/E874FC9810BFD8ADEF56F4959C632A90` doi: 10.3189/S0022143000011291

Nakaya, U. (1958). Mechanical properties of single crystals of ice. Part 1. Geometry of deformation. *SIPRE Res. Rep.*, *28*.

NEEM community members. (2013, January). Eemian interglacial reconstructed from a Greenland folded ice core. *Nature*, *493*(7433), 489–494. Retrieved 2024-05-10, from `https://www.nature.com/articles/nature11789` doi: 10.1038/nature11789

North Greenland Ice Core Project members. (2004, September). High-resolution record of Northern Hemisphere climate extending into the last interglacial period. *Nature*, *431*(7005), 147–151. Retrieved 2024-06-06, from `https://www.nature.com/articles/nature02805` doi: 10.1038/nature02805

Painer, F., Kipfstuhl, S., Drury, M., Uchida, T., Freitag, J., & Weikusat, I. (2025, October). Air clathrate hydrates in the EDML ice core, Antarctica. *The Cryosphere*, *19*(10), 5023–5044. Retrieved 2026-01-12, from `https://tc.copernicus.org/articles/19/5023/2025/` doi: 10.5194/tc-19-5023-2025

Paterson, W. S. B. (1991). Why ice-age ice is sometimes "soft". *Cold Regions Science and Technology*, *20*, 75–98.

Paterson, W. S. B. (1994). *The physics of glaciers.* Pergamon.

Peterson, J. M., Shackleton, S., Higgins, J., Severinghaus, J., Yan, Y., Buizert, C., . . . Brook, E. (2025). Ice cores from the Allan Hills, Antarctica show relatively stable atmospheric CO2 and CH4 levels over the last 3 million years. *Accepted in Nature*. Retrieved 2025-07-02, from `https://www.researchsquare.com/article/rs-5610566/v1` doi: 10.21203/rs.3.rs-5610566/v1

Petit, J. R., Jouzel, J., Raynaud, D., Barkov, N. I., Barnola, J.-M., Basile, I., . . . Stievenard, M. (1999). Climate and atmospheric history of the past 420,000 years from the Vostok ice core, Antarctica The recent completion of drilling at Vostok station in East. *Nature*, *399*, 429–436.

Qi, C., Prior, D. J., Craw, L., Fan, S., Llorens, M.-G., Griera, A., . . . Goldsby, D. L. (2019, February). Crystallographic preferred orientations of ice deformed in direct-shear experiments at low temperatures. *The Cryosphere*, *13*(1), 351–371. Retrieved 2026-01-12, from `https://tc.copernicus.org/articles/13/351/2019/` doi: 10.5194/tc-13-351-2019

Rigsby, G. P. (1960, January). Crystal Orientation in Glacier and in Experimentally Deformed Ice. *Journal of Glaciology*, *3*(27), 589–606. Retrieved 2024-01-15, from `https://www.cambridge.org/core/journals/journal-of-glaciology/article/crystal-orientation-in-glacier-and`

-in-experimentally-deformed-ice/56A54220209C982DC968633D21A371EC doi: 10.3189/S0022143000023716

Shackleton, S., Hishamunda, V., Davidge, L., Brook, E., Peterson, J. M., Carter, A., … Higgins, J. A. (2025, November). Miocene and Pliocene ice and air from the Allan Hills blue ice area, East Antarctica. *Proceedings of the National Academy of Sciences*, *122*(44), e2502681122. Retrieved 2025-11-05, from https://pnas.org/doi/10.1073/pnas.2502681122 doi: 10.1073/pnas.2502681122

Shackleton, S., Hishamunda, V., Yan, Y., Carter, A., Morgan, J., Severinghaus, J., … Higgins, J. (2025, January). *Global ocean heat content over the past 3 million years.* Retrieved 2025-07-02, from https://www.researchsquare.com/article/rs-5610580/v1 (ISSN: 2693-5015) doi: 10.21203/rs.3.rs-5610580/v1

Shoji, H., & Langway, C. C. (1985). Mechanical Properties of Fresh Ice Core from Dye 3, Greenland. In *Greenland Ice Core: Geophysics, Geochemistry, and the Environment* (pp. 39–48). American Geophysical Union (AGU).

Sinisalo, A., & Moore, J. C. (2010). Antarctic blue ice areas-towards extracting palaeoclimate information. *Antarctic Science*, *22*(2), 99–115. Retrieved 2024-11-22, from https://www.cambridge.org/core/journals/antarctic-science/article/antarctic-blue-ice-areas-towards-extracting-palaeoclimate-information/15D1D17180A65A287AB4361CCAAB946E

Sitter, L. U. d. L. U. (1964). *Structural geology.* New York, McGraw-Hill. Retrieved 2025-08-07, from http://archive.org/details/structuralgeolog0000sitt

Smith, R. B. (1975, November). Unified theory of the onset of folding, boudinage, and mullion structure. *GSA Bulletin*, *86*(11), 1601–1609. Retrieved 2025-08-06, from https://doi.org/10.1130/0016-7606(1975)86<1601:UTOTOO>2.0.CO;2 doi: 10.1130/0016-7606(1975)86⟨1601:UTOTOO⟩2.0.CO;2

Spaulding, N. E., Spikes, V. B., Hamilton, G. S., Mayewski, P. A., Dunbar, N. W., Harvey, R. P., … Kurbatov, A. V. (2012). Ice motion and mass balance at the Allan Hills blue-ice area, Antarctica, with implications for paleoclimate reconstructions. *Journal of Glaciology*, *58*(208), 399–406. Retrieved 2024-08-02, from https://www.cambridge.org/core/product/identifier/S0022143000212124/type/journal_article doi: 10.3189/2012JoG11J176

Spencer, M., Alley, R., & Fitzpatrick, J. (2006). Developing a bubble number-density paleoclimatic indicator for glacier ice. *Journal of Glaciology*, *52*(178), 358–364. Retrieved 2025-11-10, from https://www.cambridge.org/core/product/identifier/S0022143000211647/type/journal_article doi: 10.3189/172756506781828638

Stoll, N., Bohleber, P., Dallmayr, R., Wilhelms, F., Barbante, C., & Weikusat, I. (2023, September). The new frontier of microstructural impurity research in polar ice. *Annals of Glaciology*, 1–4. Retrieved 2023-09-21, from https://www.cambridge.org/core/product/identifier/S0260305523000617/type/journal_article doi: 10.1017/aog.2023.61

Stoll, N., Eichler, J., Hörhold, M., Shigeyama, W., & Weikusat, I. (2021). A Review of the Microstructural Location of Impurities and Their Impacts on Deformation. *Frontiers in Earth Science*, *8*(January). doi: 10.3389/feart.2020.615613

Stoll, N., Weikusat, I., Jansen, D., Bons, P., Darányi, K., Westhoff, J., … Kerch, J. (2025, September). Linking crystallographic orientation and ice stream dynamics: evidence from the EastGRIP ice core. *The Cryosphere*, *19*(9), 3805–3830. Retrieved 2025-09-22, from https://tc.copernicus.org/articles/19/3805/2025/ doi: 10.5194/tc-19-3805-2025

Stoll, N., Westhoff, J., Bohleber, P., Svensson, A., Dahl-Jensen, D., Barbante, C., & Weikusat, I. (2023, May). Chemical and visual characterisation of EGRIP glacial ice and cloudy bands within. *The Cryosphere*, *17*(5), 2021–2043. Retrieved 2023-05-12, from https://tc.copernicus.org/articles/17/2021/2023/ doi: 10.5194/tc-17-2021-2023

Svensson, A., Nielsen, S. W., Kipfstuhl, S., Johnsen, S. J., Steffensen, J. P., Bigler, M., . . . Röthlisberger, R. (2005). Visual stratigraphy of the North Greenland Ice Core Project (NorthGRIP) ice core during the last glacial period. *Journal of Geophysical Research*, *110*(2), 1–11. doi: 10.1029/2004JD005134

Thorsteinsson, T., Kipfstuhl, J., & Miller, H. (1997). Textures and fabrics in the GRIP ice core. *Journal of Geophysical Research: Oceans*, *102*(C12), 26583–26599. (ISBN: 2156-2202) doi: 10.1029/97JC00161

Ueltzhöffer, K. J., Bendel, V., Freitag, J., Kipfstuhl, S., Wagenbach, D., Faria, S. H., & Garbe, C. S. (2010). Distribution of air bubbles in the EDML and EDC (Antarctica) ice cores, using a new method of automatic image analysis. *Journal of Glaciology*, *56*(196), 339–348. Retrieved 2024-09-17, from https://www.cambridge.org/core/product/identifier/S0022143000208277/type/journal_article doi: 10.3189/002214310791968511

Urai, J. L., Means, W. D., & Lister, G. S. (1986). Dynamic Recrystallization of Minerals. In *Mineral and Rock Deformation* (pp. 161–199). American Geophysical Union (AGU). Retrieved 2025-09-02, from https://onlinelibrary.wiley.com/doi/abs/10.1029/GM036p0161

Wallbrecher, E. (1986). *Tektonische und gefügeanalytische Arbeitsweisen: graphische, rechnerische und statistische Verfahren.* Stuttgart: Enke.

Weertman, J., & Weertman, J. R. (1992). *Elementary Dislocation Theory.* Oxford: Oxford University Press.

Weikusat, I., Jansen, D., Binder, T., Eichler, J., Faria, S. H., Wilhelms, F., . . . Kleiner, T. (2017, February). Physical analysis of an Antarctic ice core—towards an integration of micro- and macrodynamics of polar ice. *Philosophical Transactions of the Royal Society A: Mathematical, Physical and Engineering Sciences*, *375*(2086), 20150347. doi: 10.1098/rsta.2015.0347

Weikusat, I., Kipfstuhl, S., Faria, S. H., Azuma, N., & Miyamoto, A. (2009). Subgrain boundaries and related microstructural features in EDML (Antarctica) deep ice core. *Journal of Glaciology*, *55*(191), 461–472. doi: 10.3189/002214309788816614

Wilson, C. J., Russell-Head, D. S., & Sim, H. M. (2003). The application of an automated fabric analyzer system to the textural evolution of folded ice layers in shear zones. *Annals of Glaciology*, *37*(1996), 7–17. doi: 10.3189/172756403781815401

Wilson, C. J. L., & Zhang, Y. (1994, January). Comparison between experiment and computer modelling of plane-strain simple-shear ice deformation. *Journal of Glaciology*, *40*(134), 46–55. Retrieved 2025-08-05, from https://www.cambridge.org/core/journals/journal-of-glaciology/article/comparison-between-experiment-and-computer-modelling-of-planestrain-simpleshear-ice-deformation/6823F1933E337BB2E925528E1FA26A59 doi: 10.3189/S0022143000003786

Wolff, E. W., Fischer, H., van Ommen, T., & Hodell, D. A. (2022, July). Stratigraphic templates for ice core records of the past 1.5 Myr. *Climate of the Past*, *18*(7), 1563–1577. Retrieved 2024-10-01, from https://cp.copernicus.org/articles/18/1563/2022/ doi: 10.5194/cp-18-1563-2022

Woodcock, N. H. (1977). Specification of fabric shapes using an eigenvalue method. *Geological Society of America Bulletin*, *88*, 1231–1236.

Yan, Y., Bender, M. L., Brook, E. J., Clifford, H. M., Kemeny, P. C., Kurbatov, A. V., . . . Higgins, J. A. (2019, October). Two-million-year-old snapshots of atmospheric gases from Antarctic ice. *Nature*, *574*(7780), 663–666. Retrieved 2024-08-02, from https://www.nature.com/articles/s41586-019-1692-3 doi: 10.1038/s41586-019-1692-3

Yoshida, M., Ando, H., Omoto, K., Naruse, R., & Ageta, Y. (1971, January). Discovery of Meteorites near Yamato Mountains, East Antarctica. *Antarctic Record*, *39*, 62–65.

1056 ## Appendix A Stereo-plots

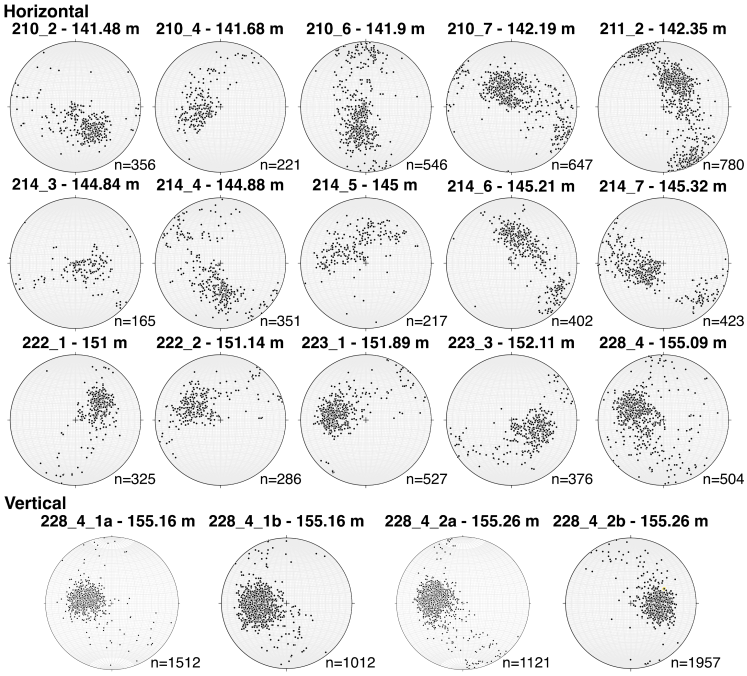

Figure A1. Stereo-plots (lower-hemisphere Schmidt equal-area projection) for all samples; n displays the number of analyzed crystals per sample. The last four samples are adjacent vertical sections; 1a and 1b are above 2a and 2b.

Appendix B Aspect Ratio Histogram

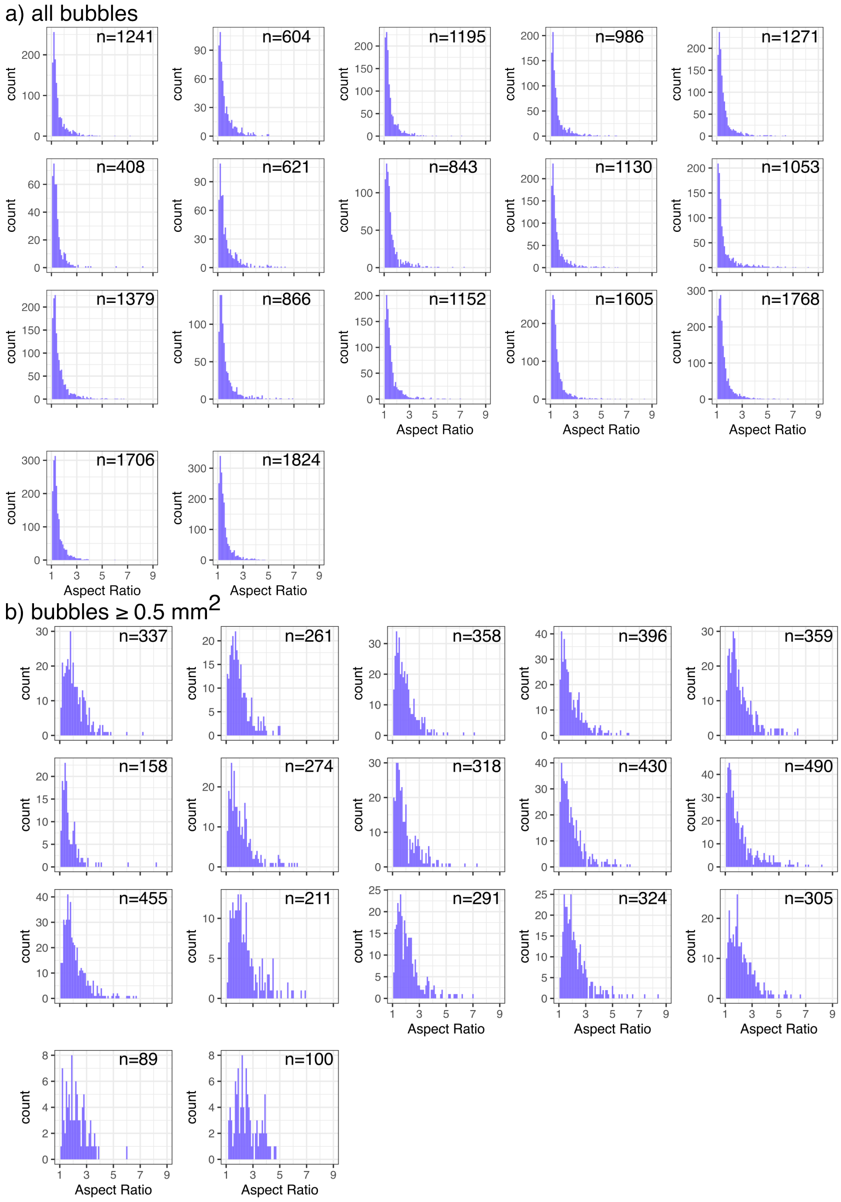

Figure B1. Aspect ratio distribution for a) all bubbles and b) bubbles greater than 0.5 mm^2. The last two plots are vertical sections 228_4_1b and 228_4_2b.

Appendix C 3D CT Bubble Data

Table C1. Overview of horizontal ALHIC1901 samples analyzed with the 3D CT. Two different 214_5 sub samples were analyzed.

Sample	Depth	Analyzed volume (cm^3)	Bubbles (n)	Bubble number density ($1/cm^3$)	Porosity (%)
210_4	141.68	9.77	535	54.76	0.47
210_7	142.19	13.44	731	54.38	0.55
214_3	144.84	5.81	202	34.74	0.38
214_4	144.88	9.74	351	36.05	0.43
214_5	145.00	10.82	1,299	120.06	0.53
214_5	145.00	17.98	948	52.72	0.52
214_6	145.32	9.84	363	36.88	0.43
222_1	151.00	14.13	862	61.02	0.45
222_2	151.14	6.47	359	55.51	0.44
228_4	155.09	4.53	380	83.88	0.32
Total/mean	-	-	6,030	59.00	0.45

1059 ## Appendix D 3D CT Aspect Ratio Histogram

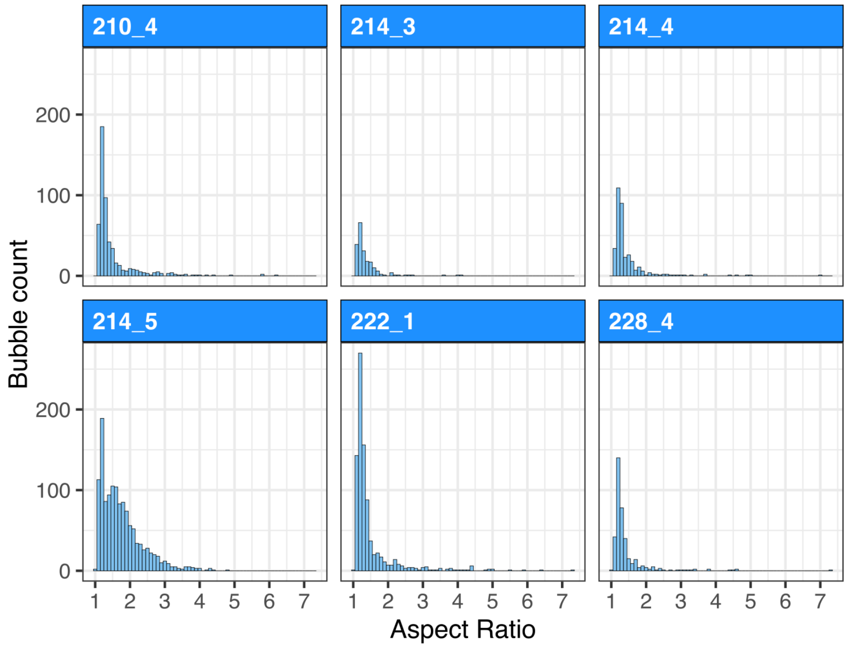

Figure D1. Representative aspect ratio distribution for six samples analyzed with the AWI 3D X-ray microfocus CT.